

Origin of the wide-angle hot H₂ in DG Tauri

New insight from SINFONI spectro-imaging

V. Agra-Amboage¹, S. Cabrit^{2,4}, C. Dougados^{3,4}, L. E. Kristensen⁵, L. Ibgui², and J. Reunanen⁶

¹ Universidade do Porto, Faculdade de Engenharia, Departamento Engenharia física, SIM Unidade FCT 4006, rua Dr. Roberto Frias s/n, 4200-465 Porto, Portugal
e-mail: vaa@fe.up.pt

² LERMA, UMR 8112 du CNRS & Observatoire de Paris, ENS, UPMC, UCP, 61 avenue de l'Observatoire, 75014 Paris, France

³ Laboratoire Franco-Chilien d'Astronomie, UMI 3386 du CNRS, 1515 Camino el observatorio, Casilla 36-D correo central, Santiago, Chile

⁴ IPAG, UMR 5274 du CNRS & Univ. Joseph Fourier, 414 rue de la Piscine, 38041 Grenoble, France

⁵ Harvard-Smithsonian Center for Astrophysics, 60 Garden Street, Cambridge MA 02138, USA

⁶ Tuorla Observatory, Department of Physics and Astronomy, University of Turku, Väisäläntie 20, 21500 Piikkiö, Finland

Received 1 October 2012 / Accepted 30 December 2013

ABSTRACT

Context. The origin of protostellar jets remains a major open question in star formation. Magnetohydrodynamical (MHD) disc winds are an important mechanism to consider, because they would have a significant impact on planet formation and migration.

Aims. We wish to test the origins proposed for the extended hot H₂ at 2000 K around the atomic jet from the T Tauri star DG Tau, in order to constrain the wide-angle wind structure and the possible presence of an MHD disc wind in this prototypical source.

Methods. We present spectro-imaging observations of the DG Tau jet in H₂ 1–0 S(1) with 0'.12 angular resolution, obtained with SINFONI/VLT. Thanks to spatial deconvolution by the point spread function and to careful correction for wavelength calibration and for uneven slit illumination (to within a few km s⁻¹), we performed a thorough analysis and modeled the morphology and kinematics. We also compared our results with studies in [Fe II], [O I], and FUV-pumped H₂. Absolute flux calibration yields the H₂ column/volume density and emission surface, and narrows down possible shock conditions.

Results. The limb-brightened H₂ 1–0 S(1) emission in the blue lobe is strikingly similar to FUV-pumped H₂ imaged 6 yr later, confirming that they trace the same hot gas and setting an upper limit <12 km s⁻¹ on any expansion proper motion. The wide-angle rims are at lower blueshifts (between –5 and 0 km s⁻¹) than probed by narrow long-slit spectra. We confirm that they extend to larger angle and to lower speed the onion-like velocity structure observed in optical atomic lines. The latter is shown to be steady over ≥4 yr but undetected in [Fe II] by SINFONI, probably due to strong iron depletion. The rim thickness ≤14 AU rules out excitation by C-type shocks, and J-type shock speeds are constrained to ≈10 km s⁻¹.

Conclusions. We find that explaining the H₂ 1–0 S(1) wide-angle emission with a shocked layer requires either a recent outburst (15 yr) into a pre-existing ambient outflow or an excessive wind mass flux. A slow photoevaporative wind from the dense irradiated disc surface and an MHD disc wind heated by ambipolar diffusion seem to be more promising and need to be modeled in more detail. Better observational constraints on proper motion and rim thickness would also be crucial for clarifying the origin of this structure.

Key words. stars: formation – stars: winds, outflows – stars: variables: T Tauri, Herbig Ae/Be – techniques: imaging spectroscopy – molecular data – infrared: stars

1. Introduction

Jets from young stars are ubiquitous in star formation, and their link with accretion processes is well established (Cabrit et al. 1990; Hartigan et al. 1995). They are launched from the inner regions of the star-disc system, the same disc that may ultimately give rise to a planetary system. Although a number of models exist for their generation (see, for example, the reviews of Ferreira et al. 2006; Shang et al. 2007; and Pudritz et al. 2007), the exact mechanism by which mass is ejected from accreting systems and collimated into jets is an open problem. It is thought that the same basic magnetohydrodynamic (MHD) mechanism is responsible for launching jets in objects as diverse as brown dwarfs (Whelan et al. 2005), post-AGB stars (e.g., García-Díaz et al. 2008; García-Segura et al. 2005), compact objects in binary systems, and perhaps even active galactic nuclei. Because of their

proximity and rich set of diagnostic emission lines, jets from young stellar objects represent a particularly useful test bed for the MHD jet-launching paradigm (see the reviews of Bally et al. 2007; Ray et al. 2007).

Molecular hydrogen is the primary gas constituent in the circumstellar environment of young stars. The $v = 1-0$ S(1) transition of H₂ at 2.12 μm is often detected in embedded protostars, with the emission formed primarily in shock-excited collimated outflows (e.g., Davis et al. 2011, 2002). The presence of H₂ in jets might be an indication that MHD ejection operates out to disc radii ≥0.2–1 AU where molecules can survive against dissociation (Safier 1993; Panoglou et al. 2012). If such extended MHD disc winds persist until the later planet building phase, they could maintain fast accretion across the disc “dead-zone” where ionization in the midplane is too low to activate MHD turbulence (Bai 2013). The associated magnetic fields would have

strong consequences for the formation and migration of planets (Fromang et al. 2005; Bai & Stone 2013). The H₂ emission from warm ($T = 1000\text{--}3000\text{ K}$) gas was recently detected within 100 AU of more evolved T Tauri stars (TTSs) and Herbig Ae/Be stars, both in the near-infrared and far-ultraviolet (FUV) domains (e.g., Valenti et al. 2000; Ardila et al. 2002; Bary et al. 2003; Carmona et al. 2011). When studied at high spectral resolution, these lines split into two populations: most show narrow profiles centered on the stellar velocity, suggesting an origin in a warm disc atmosphere (quiescent H₂), but $\approx 30\%$ of them display profiles blueshifted by $10\text{--}30\text{ km s}^{-1}$, sometimes with blue wings extending up to -100 km s^{-1} , suggesting formation in an outflow (Takami et al. 2004; Herczeg et al. 2006; Greene et al. 2010; Carmona et al. 2011; France et al. 2012). In particular, long-slit spectra of DG Tau provide evidence of a warm H₂ outflow at $\approx -20\text{ km s}^{-1}$, shifted by $\approx 30\text{ AU}$ along the blue jet direction and with an estimated width $\approx 80\text{ AU}$ (Takami et al. 2004; Schneider et al. 2013b). Beck et al. (2008) conducted a 2D spectro-imaging study of H₂ rovibrational lines in six CTTs known to be associated with large scale atomic jets, including DG Tau, and found spatially extended emission in all cases, with sizes up to 200 AU. While the data are not flux calibrated, relative level populations among *K*-band H₂ lines indicate excitation temperatures in the range 1800–2300 K. From various arguments, Takami et al. (2004) and Beck et al. (2008) argue that the H₂ properties are in general not well explained by FUV or X-ray irradiation and are most consistent with shock-excited emission from the inner regions of the atomic jets or from wider-angle winds encompassing these flows. Takami et al. (2004) also mention ambipolar diffusion on the outer molecular streamlines of an MHD disc wind as an alternative heating mechanism for the warm H₂ outflow in DG Tau. Schneider et al. (2013a) also favor a molecular MHD disc wind, but heated by shocks rather than by ambipolar diffusion. In HL Tau, on the other hand, Takami et al. (2007) interpret the V-shaped H₂ emission encompassing the atomic jet as a shocked cavity driven into the envelope by an unseen wide-angle wind. In any case, extended H₂ emission in TTS clearly holds key information on their wide-angle wind structure, the radial extension of any MHD disc wind present, and its impact on protoplanetary disc physics.

In an effort to extract this information, we present in this paper an in-depth analysis of H₂ ro-vibrational 1–0 S(1) emission associated with DG Tauri, using flux-calibrated spectro-imaging *K*-band observations with $0''.12$ resolution conducted with SINFONI/VLT. This work complements our detailed study of the atomic flow component and accretion rate in DG Tau based on [Fe II] lines in *H*-band and Bry in *K*-band, observed at the same epoch with the same instrument (Agra-Amboage et al. 2011, hereafter Paper I). Our analysis improves on that in Beck et al. (2008) in several ways: We apply spatial deconvolution to obtain a sharper view of the brightness distribution, and perform careful correction for wavelength calibration and uneven-slit illumination to retrieve radial velocities along and across the jet axis down to a precision of a few km s^{-1} . This allows us to conduct a detailed comparison with the spatio-kinematic structure of the atomic flow component and FUV H₂ emission in DG Tau, and to constrain both the proper motion and the 3D velocity field of warm H₂, including rotation. In addition, the absolute flux-calibration of the 1–0 S(1) line is used to infer column densities and emitting surfaces and, together with its ratio to 2–1 S(1) at $2.25\text{ }\mu\text{m}$, to restrict the possible shock parameters for H₂ excitation. We then combine this new information to critically re-examine the main scenarios that have been invoked for the origin of wide-angle H₂ emission in DG Tau and other

TTS, namely: (1) an irradiated disc/envelope; (2) a molecular MHD disc wind heated by ambipolar diffusion; (3) a forward shock sweeping up the envelope; (4) a reverse shock driven back into a wide-angle molecular wind. The paper is organized as follows: The observations, data reduction procedure, and centroid velocity measurements are described in Sect. 2. In Sect. 3, we present the new results brought by our observations on the morphology, kinematics, and column density of the wide-angle H₂, and compare with the atomic and FUV H₂ emission properties. In Sect. 4, we clarify the shock parameters that could explain the H₂ surface brightness and line ratio, we explore the possible 3D velocity fields, and we discuss the strengths and weaknesses of various proposed origins for the wide-angle H₂. Our conclusions are summarized in Sect. 5. Throughout the paper we assume a distance of 140 pc to the object.

2. H₂ observations, data reduction, and velocity measurements

Observations of the DG Tau microjet in *K* band were conducted on 15 October 2005 at the Very Large Telescope (VLT), using the integral field spectrograph SINFONI combined with an adaptive optics (AO) module (Eisenhauer et al. 2003; Bonnet et al. 2004). The field of view is $3'' \times 3''$ with a spatial sampling of $0''.05 \times 0''.1$ per “spaxel”. The smallest sampling is along the direction of the slicing mirrors (denoted as *X*-axis in the following) and is aligned perpendicular to the DG Tau jet axis, i.e., at PA = 45°. After AO correction, the effective spatial resolution achieved in the core of the point spread function (PSF) is $\sim 0''.12$ (FWHM of a Gaussian fit to the reconstructed continuum image). The spectral configuration used provides a dispersion of 0.25 nm/pixel over a spectral range of $1.95\text{ }\mu\text{m}$ to $2.45\text{ }\mu\text{m}$. The spectral resolution as determined from OH sky lines is $\sim 88\text{ km s}^{-1}$ (median FWHM), with smooth systematic variations of $\pm 15\text{ km s}^{-1}$ along the *Y*-axis. Three datacubes of 250 s each were obtained, one on sky and two on source (referred to as exposure 1 and exposure 2 hereafter).

The standard data reduction steps were carried out using the SINFONI pipeline. Datacubes are corrected for bad pixels, dark, flat field, geometric distortions on the detector, and sky background. An absolute wavelength calibration based on daytime arclamp exposures is also performed by the SINFONI pipeline. However, the accuracy is insufficient for kinematical studies of stellar jets. Unlike for the *H*-band data of Paper I, the OH sky lines in our *K*-band sky exposure have too low signal-to-noise ratio (S/N) to provide a reliable improvement. Instead, we rely here on absorption lines of telluric and photospheric origin against the strong DG Tau continuum. Telluric lines near the H₂ 1–0 S(1) line were identified from comparison with a simulated atmospheric absorption spectrum convolved to our spectral resolution, generated with an optimized line-by-line code tested against laboratory measurements (Ibgui & Hartmann 2002; Ibgui et al. 2002), using molecular data from the HITRAN database (Rothman et al. 2009). Two unblended H₂O lines strong enough for velocity calibration were identified: one at $\approx 2.112\text{ }\mu\text{m}$ (4735.229 cm^{-1}), and one at $\approx 2.128\text{ }\mu\text{m}$ (4699.750 cm^{-1}). Three photospheric lines are also present on the blue side of the H₂ 1–0 S(1) line (Wallace & Hinkle 1996): a Mg doublet at $\approx 2.107\text{ }\mu\text{m}$ (4746.841 and 4747.097 cm^{-1}) and two Al lines at $\approx 2.110\text{ }\mu\text{m}$ and $\approx 2.117\text{ }\mu\text{m}$ (4739.598 and 4723.769 cm^{-1}). All three are well detected in the DG Tau spectrum (see also Fischer et al. 2011), but since the Mg line is a doublet we only use the two Al lines for velocity calibration. In each exposure, the centroids of the two Al photospheric lines

and two H₂O telluric lines were determined by Gaussian fitting on a high S/N reference spectrum obtained by averaging spaxels over $\pm 0''.5$ along the slicing mirror closest to the DG Tau continuum peak (centered at $Y = 0$ in exposure 1 and $Y = 0''.03$ in exposure 2). After correcting photospheric lines for the motion of DG Tau ($V_{\text{hel}} = 16.5 \text{ km s}^{-1}$, Bacciotti et al. 2000), the four velocity shifts were fitted by a linear function of wavelength to derive the global calibration correction to apply at $2.12 \mu\text{m}$. The maximum deviation between the 4 data points and the linear fit is $\leq 2 \text{ km s}^{-1}$ in each exposure, and we take this as an estimate of the maximum error in our absolute calibration.

The H₂ 1–0 S(1) emission profiles in each exposure are then continuum-subtracted and corrected for telluric absorption following the procedure described in Paper I: We select a high S/N reference “photospheric” spectrum with no discernable H₂ line at our resolution (at $\Delta x \sim 0''$, $\Delta y \sim 0''$). This reference spectrum is scaled down to fit the local continuum level of each individual spaxel, and subtracted out. This ensures optimal accuracy in the removal of telluric and photospheric absorption features (cf. Fig. 1 in Paper I); it will also remove the PSF of any faint H₂ emission present in the reference position, but the extended emission beyond $0''.1$ of the star will not be affected. The same procedure is applied to extract the 2–1 S(1) line profiles. Correction for atmospheric differential diffraction is then done by registering each H₂ datacube on the centroid position of the nearby continuum, as calculated by a Gaussian fit in the X and Y directions of the reconstructed continuum image. The data are flux-calibrated on the standard star HD 28107, with an estimated error of 5%.

H₂ centroid velocities are determined by a Gaussian fit to the extracted line profile. The fitted centroids are subject to a random fitting error due to noise, given by $1\sigma \approx FWHM/(2.35 S/N)$ for a Gaussian of width FWHM and signal-to-noise ratio S/N at the line peak (Porter et al. 2004). Monte-Carlo simulations show that this error can be much smaller than the velocity sampling (Agra-Amboage et al. 2009). The FWHM of fitted Gaussians show the same systematic variations with Y -offset as OH sky lines and indicate a small intrinsic width $\Delta V \leq 30 \text{ km s}^{-1}$ for the H₂ emission, in agreement with higher resolution spectra (Takami et al. 2004; Schneider et al. 2013b).

After global absolute wavelength calibration, velocity centroids are still subject to small residual instrumental calibration drifts along/across slicing mirrors. Our simultaneous sky exposure has too low S/N to correct for this effect. We thus estimate its typical magnitude using bright OH lines near $2.12 \mu\text{m}$ in two high S/N K -band sky datacubes obtained in the same instrumental configuration, during a different run. Along each slicing mirror, i.e., transverse to the jet axis, the centroids shifts are mainly caused by a systematic residual slope, with random fluctuations $< 1 \text{ km s}^{-1}$ on top of it. After averaging along each mirror (i.e., when building a PV diagram along the jet axis), the OH centroids show random drifts from row to row with an rms of $0.5\text{--}0.8 \text{ km s}^{-1}$. The resulting overall distribution of OH line centroids among individual spaxels in the field of view is essentially Gaussian, with an rms of 1.5 km s^{-1} . We will include the relevant random dispersion in our error bars on H₂ centroid velocities, and also take into account the systematic “slope effect” along slicing mirrors when searching for transverse rotation signatures (see Sect. 3.2.3).

Finally, the H₂ velocity centroids need to be corrected for spurious velocity shifts due to uneven-slit illumination. Indeed, the slicing mirrors in SINFONI behave like a long-slit spectrograph where off-axis light suffers from a shift in wavelength on the detector with respect to on-axis light. The magnitude of

this effect depends on the gradient of light distribution within the “slitlet”, and in principle can be as high as the spectral resolution. In our observations, the total light distribution is dominated by the PSF of the stellar continuum, whose FWHM is on the order of the “slitlet” width ($0.1''$) therefore one might expect this effect to be significant. However, the AO system does not provide full correction for atmospheric seeing on DG Tau, so that most of the flux in the PSF is not in the Gaussian core but in broader wings with smoother gradients. As we demonstrate in Appendix A, the spurious velocity shifts in such conditions remain small (a few km s^{-1}). Furthermore, they can be modeled and corrected for with good accuracy, with an estimated residual error of $\leq 2 \text{ km s}^{-1}$, and even better in the blue lobe beyond $-0''.3$ from the star. All velocities in this paper are corrected for uneven slit illumination using the model outlined in Appendix A, and expressed in the reference frame of the star assuming $V_{\text{hel}} = 16.5 \text{ km s}^{-1}$ (Bacciotti et al. 2000).

3. Results

3.1. H₂ 1–0 S(1) morphology and comparison with FUV and [Fe II] data

The top left panel of Fig. 1¹ shows the raw continuum-subtracted map in the H₂ 1–0 S(1) line² where the two on-source exposures were combined to increase S/N. The morphology agrees with that first reported by Beck et al. (2008) in the same line at comparable resolution, namely: a bright cusp on the blue side (negative ΔY), a fainter broader arc on the red side at $+0''.6\text{--}1''$ from the star, and a dark lane in between, presumably due to occultation by the circumstellar disc of DG Tau. The dark lane was previously seen in optical and H -band observations of the DG Tau jet, and the inferred disc size and extinction found consistent with disc properties from dust continuum maps (see Lavalley et al. 1997; Pyo et al. 2003, and Paper I).

To give a sharper view of the morphology, the raw image was deconvolved by the continuum image, used as an estimate of the contemporary point spread function (PSF). We used the LUCY restoration routine implemented in the STSDAS/IRAF package. The derived image did not change significantly after 40 iterations. The advantage of deconvolution is mainly to suppress the strong extended non-Gaussian wings of the PSF caused by partial AO correction. The final resolution is not precisely known but, given our limited spatial sampling, is probably close to our Gaussian PSF core before deconvolution ($0''.12$ FWHM).

The deconvolved image of the blue lobe is presented in the bottom left panel of Fig. 1. Bright H₂ 1–0 S(1) emission appears confined to a small roundish region of about $0''.5 = 75 \text{ AU}$ in diameter. The emission is clearly limb-brightened, suggesting a “hollow cavity” geometry. It is brighter on the side facing the star, and extends sideways up to $\pm 0''.2$ from the jet axis before closing back. A bright peak is also seen along the jet axis at $\Delta Y \approx -0''.1$, and a fainter one at $\Delta Y \approx -0''.4$. Note that we may be underestimating the flux within $< 0''.1$ of the star due to our procedure for continuum and telluric removal (see

¹ Figures 1–3, 6–10, B.1, and B.2 are available in colour in electronic form.

² Because the spectral response of SINFONI is non-Gaussian and includes broad “shoulders” that may lie below the noise level, we integrated the line flux only over the three brightest velocity channels at -35.61 , -0.61 and $+34.38 \text{ km s}^{-1}$. A factor of 1.4 was then applied in order to account for the flux lost in these spectral wings (as estimated on the brightest positions in our map).

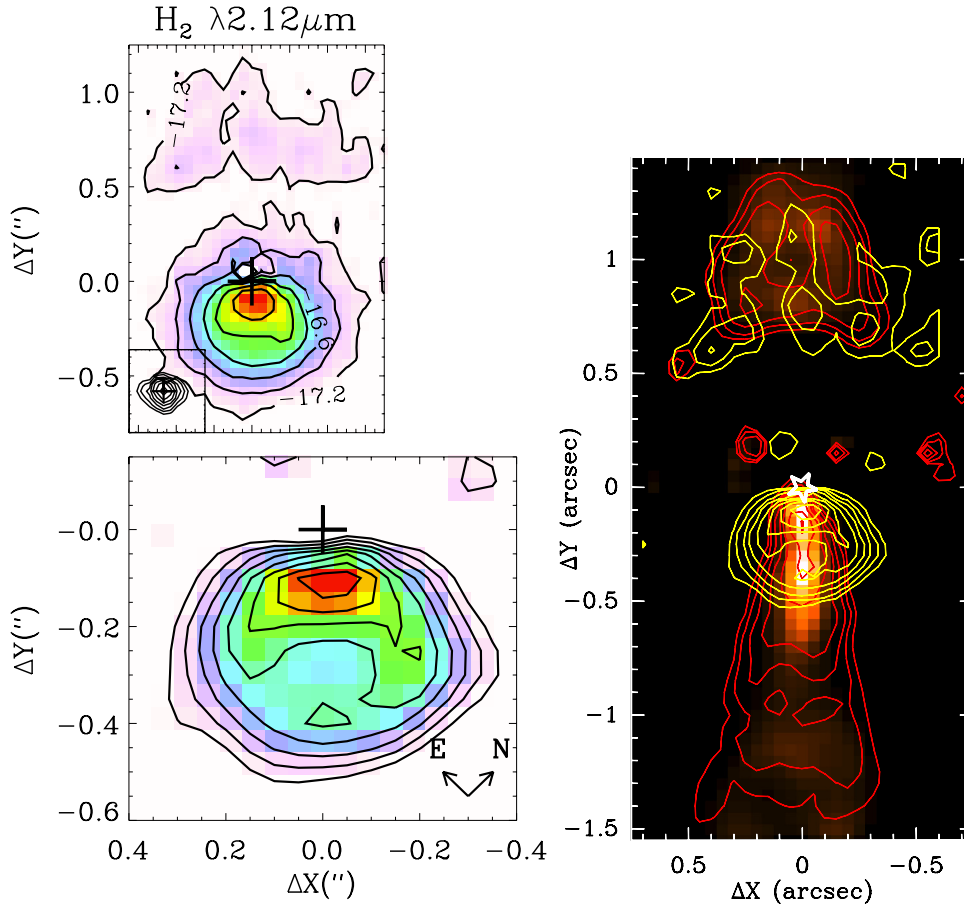


Fig. 1. *Top left:* raw continuum-subtracted map of H₂ 1–0 S(1) line emission in DG Tau. Contours start at 2.7×10^{-4} erg s⁻¹ cm⁻² sr⁻¹ and increase by factors of 2. The cross denotes the centroid of the continuum image (shown as an *insert*). *Bottom left:* H₂ 1–0 S(1) map after deconvolution by the continuum image. The lack of H₂ emission at the central position results from our continuum subtraction procedure. *Right panel:* deconvolved H₂ 1–0 S(1) image (yellow contours) superimposed on the deconvolved channel maps of [Fe II] 1.64 μm obtained at the same epoch and resolution by [Agra-Amboage et al. \(2011\)](#), in two velocity ranges: MV (red contours; $-160 \text{ km s}^{-1} < V < 120 \text{ km s}^{-1}$) and HV (background colour image; $V < -160 \text{ km s}^{-1}$ and $V > 120 \text{ km s}^{-1}$).

Sect. 2). With this limitation in mind, the morphology of our deconvolved 1–0 S(1) image is strikingly similar to the FUV image of Ly α -pumped H₂ obtained in July 2011 by [Schneider et al. \(2013a\)](#), and confirms their conclusion that the H₂ wide-angle emission in DG Tau appears essentially stationary over 6 years. We find that the bright H₂ rims near the base expanded by less than 0'.1 between the two epochs, implying a proper motion expansion speed $V_{\text{exp}} < 12 \text{ km s}^{-1}$. Dedicated monitoring in the same instrumental setup would be necessary to get a more accurate proper motion value. Nevertheless, the current limit already sets tight constraints on scenarios where the H₂ emission would originate from the interaction of a wide-angle wind with circumstellar gas (see Sect. 4).

In the top panel of Fig. 2 we plot a cut of the surface brightness of H₂ 1–0 S(1) emission along the blue jet axis as a function of distance from the source, both before and after deconvolution by the continuum. The overall flux decrease with distance is very similar to that observed in H₂ FUV emission (see Fig. 4 of [Schneider et al. 2013a](#)). The ratio of 1–0 S(1) to FUV H₂ lines thus appears roughly constant with distance. The mean brightness level towards the cavity center remains about the same before and after deconvolution, $\approx 3 \times 10^{-3}$ erg s⁻¹ cm⁻² sr⁻¹ and is therefore very robust. The peak brightness is more uncertain, since deconvolution has a bias to enhance peaks at the expense of extended lower-level emission beyond -0'.4 from the source.

We will use the peak brightness before deconvolution as a safe lower-limit.

In the right-hand panel of Fig. 1, we compare the H₂ 1–0 S(1) morphology with contemporaneous images from Paper I of the atomic jet in [Fe II] 1.64 μm in medium-velocity (MV: $-160 \text{ km s}^{-1} < V < 120 \text{ km s}^{-1}$) and high-velocity (HV: $V < -160 \text{ km s}^{-1}$ and $V > 120 \text{ km s}^{-1}$) intervals. In the red lobe, H₂ follows well the base of the bowshock feature seen in the MV range of the [Fe II] emission, suggesting that it traces the low-velocity non-dissociative wings of this bowshock. In the blue lobe, in contrast, the bright rims of H₂ emission are much broader than the [Fe II] jet, that they largely encompass. This is further quantified in the bottom panel of Fig. 2, where we plot the transverse FWHM of the H₂ 1–0 S(1) emission in the blue lobe, as measured on the deconvolved image, as a function of distance from the source. The width at $\approx -0'.1$ is dominated by the bright inner peak, which is only marginally resolved transversally. Beyond this point, the width increases up to 0'.5 at a distance of -0'.25, indicating an apparent half-opening angle $\approx 45^\circ$ similar to that determined by [Schneider et al. \(2013a\)](#) from their FUV image. This is much wider than the 14° and 4° measured at the same epoch for the MV and HV channel maps of [Fe II] (see Fig. 2 and Paper I). At larger distances, the roundish shape of the H₂ emission makes its FWHM decrease again, while the [Fe II] jet keeps its narrow opening.

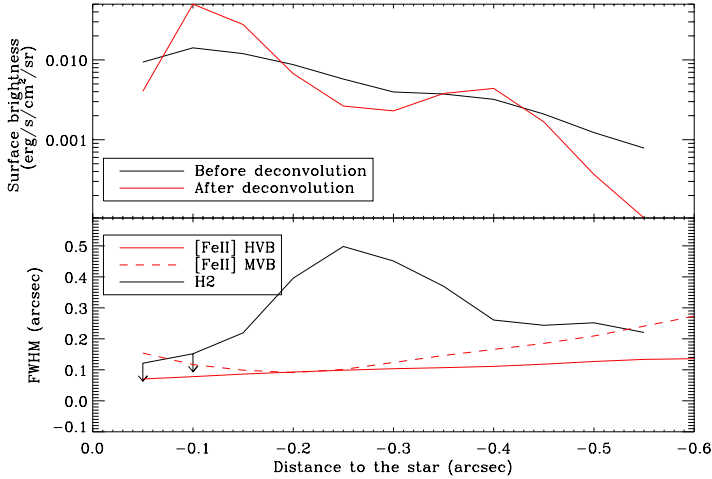


Fig. 2. *Top panel:* cut of H₂ 1–0 S(1) surface brightness along the blue jet axis, before and after deconvolution by the PSF. The drop in flux inside $-0''.1$ results from our continuum subtraction procedure. Deconvolved peak values should be viewed with caution. *Bottom panel:* transverse FWHM of H₂ 1–0 S(1) emission in the blue lobe as a function of the distance to the star, as measured in the deconvolved image. In red, we superimpose the FWHM of [Fe II] $1.64\ \mu\text{m}$ at the same epoch in two velocity ranges: MVB ($-160\ \text{km s}^{-1} < V < +50\ \text{km s}^{-1}$) and HVB ($V < -160\ \text{km s}^{-1}$), taken from Paper I.

In contrast to the marked difference in width between H₂ and [Fe II], Beck et al. (2008) noted that the V-shaped H₂ emission in DG Tau appears morphologically similar to the low-velocity blueshifted [S II] emission mapped in 1999 with HST by Bacciotti et al. (2000). (Schneider et al. 2013a) noted that the latter actually appears to fill-in the “voids” in the limb-brightened FUV H₂ emission, and concluded that the H₂ “cavity” is not really hollow but filled by low-velocity atomic flow. A limitation to this argument is that the [S II] HST maps were taken 6–12 years before the H₂ near-infrared and FUV images, respectively, while the crossing time at $50\ \text{km s}^{-1}$ from the axis to the H₂ rim is only 3 years. Data obtained closer in time are thus necessary to confirm this conclusion. In Sect. 3.2.2 we present such a comparison both in space and velocity using transverse long-slit [O I] data acquired by Coffey et al. (2007) only 2 years before our SINFONI data.

3.2. H₂ 1–0 S(1) kinematics

3.2.1. 2D velocity map and 1D velocity gradients along the jet

Figure 3 presents a 2D map of the centroid velocities for exposure 2, computed as detailed in Sect. 2. Contours of S/N are superposed to quantify the centroid Gaussian fitting error in each spaxel. This term generally dominates over the uncertainties due to instrumental drifts from spaxel to spaxel ($1.5\ \text{km s}^{-1}$ rms), uneven-slit illumination correction ($\leq 2\ \text{km s}^{-1}$), and absolute calibration ($< 2\ \text{km s}^{-1}$). Consistent results are found for exposure 1, considering the slightly different spaxel positions with respect to the central source.

Figure 3 shows that most of the area in the blue lobe is at low radial velocity, with a typical value $\approx -5\ \text{km s}^{-1}$ towards the cavity center. This is in line with the low median velocity barycenter of $-2.4\ \text{km s}^{-1}$ reported by Beck et al. (2008) in their comparable spectro-imaging study. At the same time, we find a spatially limited region of higher blueshifts close to the star that appears

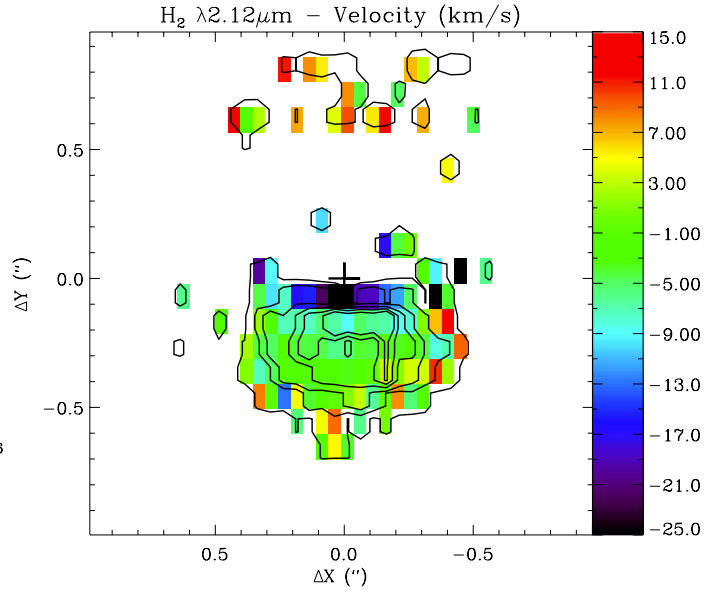


Fig. 3. Colour map of centroid velocity of the H₂ 1–0 S(1) line resulting from a one-component Gaussian fit to each individual spectrum, and corrected for uneven slit illumination. Only spaxels with $S/N > 5$ are shown. The cross marks the position of the star. Contours of $S/N = 5, 10, 15, 25, 35, 45$ are superimposed in black; the fitting error due to noise is $1\sigma \approx (40/S/N)\ \text{km s}^{-1}$ (see text and Sect. 2).

consistent with previous long-slit data in this region. The highest blueshift of $\approx -25 \pm 3\ \text{km s}^{-1}$ (at $\Delta Y = -0''.07$ and $\Delta X < \pm 0''.1$) is in excellent agreement with the $-30 \pm 4\ \text{km s}^{-1}$ observed at the same position in FUV H₂ lines in a $0''.2$ wide slit (Schneider et al. 2013b). SINFONI spectra integrated over the same slit aperture as Takami et al. (2004) also show centroids compatible with their reported radial velocity in 1–0 S(1) of $-15 \pm 4\ \text{km s}^{-1}$ (namely: $-8.5 \pm 3\ \text{km s}^{-1}$ in exposure 1 and $-7 \pm 4\ \text{km s}^{-1}$ in exposure 2, including errors in absolute calibration and uneven slit correction). The only apparent difference with long-slit data is at $\Delta Y \approx -0''.3$, where our centroid on-axis $\approx -5 \pm 4\ \text{km s}^{-1}$ is significantly lower than the $-20 \pm 6\ \text{km s}^{-1}$ reported by Schneider et al. (2013b). This may be understood by noting that the narrow $0''.2$ HST slit is dominated by a small axial H₂ knot (cf. the FUV image of Schneider et al. (2013a)), while our velocity centroids are measured on the raw (not deconvolved) SINFONI datacubes with large non-Gaussian PSF wings, and are thus heavily contaminated by the much brighter H₂ rims at wider angles. The axial H₂ knot could also be time variable. Overall, our data show that most of the wide-angle H₂ emission towards the blue lobe is at significantly lower radial velocity than inferred from long-slit spectra.

In order to increase precision on velocity gradients along the flow and in the redshifted lobe, we increased S/N by building for each exposure a position–velocity (PV) diagram along the jet in a pseudo-slit of $1''$ width, keeping the original Y-sampling along the jet axis defined by the positions of the SINFONI slicing mirrors. The faint spectra at distances farther than $-0''.7$ (blue side) and between the star and $+0''.5$ (“dark lane” on the red side) were further averaged to increase S/N. We carried out the analysis individually for each exposure; since their corrections for absolute calibration and uneven slit-illumination differ (see Sect. 2), comparison of the results gives a useful cross-check, while also improving spatial sampling of velocity gradients along the jet axis, where the slicing mirror width ($0''.1$) undersamples the core of the PSF ($0''.12$ FWHM).

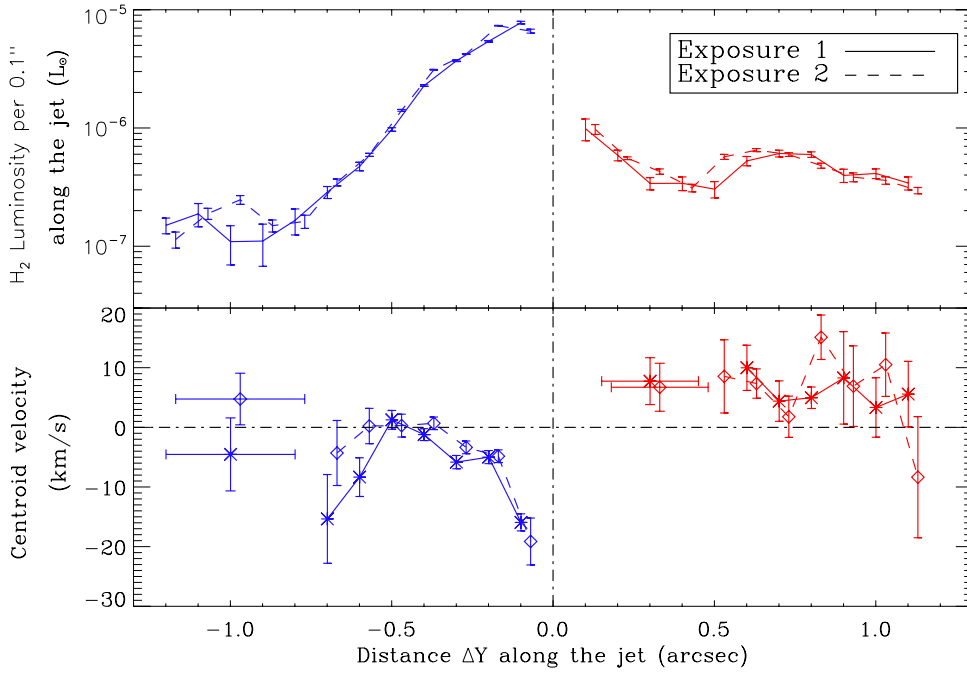


Fig. 4. *Top:* luminosity of H₂ 1–0 S(1) per 0′.1 length along the jet, integrated over 1′′ across the jet, for each exposure. *Bottom:* Gaussian-fitted centroid velocity of H₂ 1–0 S(1) in spectra averaged across a 1′′ wide pseudo-slit. Correction for uneven slit-illumination was applied to each averaged spectrum (see Appendix A). Absolute velocity calibration is better than 2 km s^{−1} in each exposure. Vertical 1σ error bars include the fitting error due to noise, and 0.8 km s^{−1} rms instrumental calibration drifts between slicing mirrors (see Sect. 2). Horizontal error bars indicate where spectra were further averaged along the jet to increase S/N.

The top panel of Fig. 4 plots the luminosity inside each “slice” of the PV diagram. The bottom panel of Fig. 4 plots the H₂ centroid velocities fitted to spectra averaged across the jet as a function of distance along the jet, for each exposure separately. The two individual exposures show excellent agreement within the error bars, giving us confidence in our velocity determinations and error estimates. The velocity gradient along the blue lobe seen in Fig. 3 is confirmed: the 1D-averaged H₂ centroids show an apparent deceleration from ≈ -18 km s^{−1} at $\Delta Y \approx -0′.1$ to ≈ -5 km s^{−1} at $-0′.2$, and to essentially zero near the cavity end at $\Delta Y = -0′.5$. This gradient is clearly too strong to be caused by measurement uncertainties; residual errors in uneven slit illumination correction are at most 2 km s^{−1} within $-0′.3$ from the star, and appear negligible further out (cf. Appendix A), while residual errors in absolute calibration would only shift each curve without affecting the gradients.

In the fainter region beyond the cavity edge, both exposures show a trend for an increased blueshift at ≈ -10 km s^{−1} at $\Delta Y \approx -0′.6$, that might be tentative evidence for a more distant faint H₂ knot along the jet axis. This position corresponds to the tip of the bright [Fe II] HVC jet beam in Fig. 1. Even fainter H₂ emission is detected around $-1′′$, with centroid velocities close to zero. A faint bubble feature is seen at this position in [Fe II] HV and MV (see Fig. 1 and Paper I). Finally, the H₂ emission in the red lobe appears mostly redshifted, with a mean radial velocity $\approx +5$ km s^{−1}. In the rest of this paper, we focus on the bright wide-angle H₂ cavity in the blue lobe, as the remaining H₂ features have too low S/N for more detailed analysis.

3.2.2. Comparison with kinematics in atomic lines

The velocity range of [Fe II]1.64 μm emission in the blue lobe of DG Tau appears totally distinct from that of H₂. The [Fe II]1.64 μm SINFONI spectra in the region of the H₂ cavity have centroids ranging from -150 to -200 km s^{−1} (Paper I). A higher resolution long-slit [Fe II]1.64 μm spectrum obtained in 2001 by Pyo et al. (2003) reveals a separate lower-velocity component peaked around -50 to -100 km s^{−1}, but still very weak

emission in the velocity range of H₂ 1–0 S(1), and an apparent acceleration away from the star in opposite sense to the centroid gradient observed in H₂. Together with the much narrower opening angle of [Fe II] compared to H₂ 1–0 S(1) (cf. Sect. 3.1) this appears to suggest no direct dynamical interaction between the [Fe II] jet and the wide-angle H₂ in DG Tau. The same kinematic and spatial separation between [Fe II] jet and H₂ wide angle emission was observed previously in the case of HL Tau by Takami et al. (2007), who then interpreted the V-shaped H₂ as a shocked outflow cavity swept-up by an unseen wide-angle wind.

In the case of DG Tau, previous optical spectro-imaging in [O I] and [S II] do provide direct evidence for a wide-angle atomic wind, with a decreasing velocity from axis to edge (Lavalley-Fouquet et al. 2000; Bacciotti et al. 2000, 2002). However, these optical data were taken 6–7 years before the SINFONI H₂ data, at a time when the DG Tau jet exhibited very high-velocity emission up to -350 km s^{−1} that was not observed since then. This makes a comparison between the two datasets somewhat uncertain. In order to investigate the spatio-kinematic relationship between the wide-angle H₂ and the atomic flow using data as close in time as possible, we compare in Fig. 5 the transverse velocity structure at $\Delta Y = -0′.3$ across the blue jet in the 1–0 S(1) line (from this paper), in the [Fe II] 1.64 μm line observed simultaneously (from Paper I) and in the optical [O I]λ6300 Å line observed only 2 years earlier with HST/STIS (from Coffey et al. 2007). The [O I] profiles were fitted by two Gaussians by Coffey et al. (2007): a “high-velocity component” (HVC) and a “low-velocity component” (LVC). Both centroids are reported in the figure. The [Fe II] profiles are narrower and under-resolved by SINFONI. They were thus fitted by single Gaussians, dominated here by the HVC.

Figure 5 shows that while the [O I] HVC coincides in velocity and spatial width with the narrow [Fe II] HVC, the [O I] LVC is much slower and spatially broader; its radial velocity drops from -60 km s^{−1} on-axis to -25 km s^{−1} at $\pm 0′.25$ from the axis, and the spatial FWHM is $\approx 0′.2$ (Coffey et al. 2008). Therefore, the [O I] LVC is filling-in the “gap” between [Fe II] and H₂ emission, both spatially and kinematically. In addition, we note

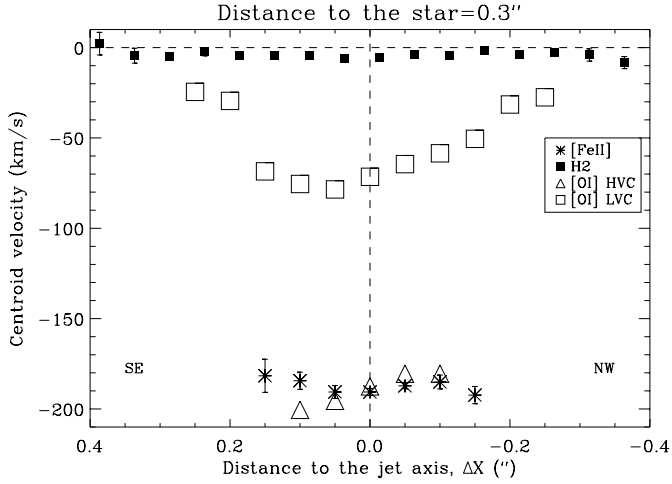


Fig. 5. Centroid velocity versus distance from the jet axis for H₂ 1–0 S(1) (filled squares, this paper), [FeII] 1.64 μm (stars, from Paper I) and [OI]λ6300 Å HVC and LVC (open symbols, from Coffey et al. 2007), all measured along a 0′.1-wide transverse cut at ΔY = −0′.3 from the star into the blue lobe. Positive ΔX is to the SE.

that the centroid variations and spatial FWHM of the [OI] LVC observed in 2003 by Coffey et al. (2008) are identical to measurements obtained 4 years earlier at the same distance from the star (see Fig. 1 in Bacciotti et al. 2002, and Fig. 14 in Maurri et al. 2013). We thus find that the spatio-kinematic structure of the LVC remains remarkably stable over more than a transverse crossing time, despite strong variability of the HVC at velocities ≥ 300 km s^{−1}. This finding definitely strengthens conclusions based on earlier 1999 HST data that the wide-angle H₂ cavity in DG Tau appears as a slower, outer extension of the “onion-like” velocity structure of the atomic flow (Takami et al. 2004; Beck et al. 2008; Schneider et al. 2013a).

Another important implication of this comparison is that [Fe II] emission does not appear as a good tracer of the wide angle atomic flow slower than 50 km s^{−1}. While Pyo et al. detect [Fe II] LVC emission within $\pm 0.15''$ of the jet axis at velocities bluer than -50 km s^{−1}, the comparison of transverse PV diagrams in [Fe II] and [O I] (see Fig. 5 of Paper I) shows no detectable contribution in [Fe II] from the wider angle, slower gas below -50 km s^{−1} that so clearly stands out in [O I] (and [S II]). This difference cannot be explained by gradients in density or temperature: the [Fe II] 1.64 μm line has a critical density intermediate between that of [O I] and [S II], and a similar upper level energy. We propose that it is due instead to iron being increasingly depleted at lower speeds. Indeed, modeling of the [Fe II] to [O I] line ratio in Paper I indicates a higher average gas-phase iron depletion of a factor 10 in the interval -100 to $+10$ km s^{−1}, compared to only a factor 3 in the interval -250 to -100 km s^{−1}. Depletion could be so high in the velocity range -50 to -25 km s^{−1} that the corresponding wide-angle emission seen in [O I] and [S II] remains undetectable in [Fe II] at the sensitivity and resolution of SINFONI.

3.2.3. Constraints on H₂ rotation

The LVC centroids in optical forbidden lines are known to display clear asymmetries between opposite sides of the jet axis, with amplitude and sign consistent with a rotating, steady magneto-centrifugal disc wind launched out to ≈ 3 AU (Bacciotti et al. 2002; Anderson et al. 2003; Pesenti et al. 2004; Coffey et al. 2007, cf. Fig. 5). We therefore make use of our SINFONI data

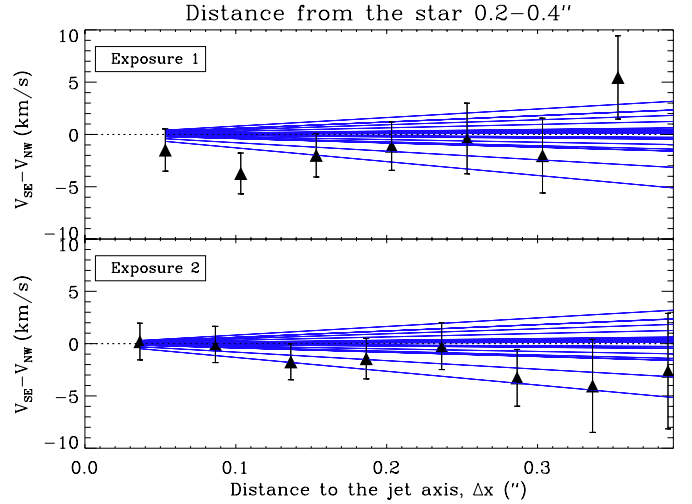


Fig. 6. Velocity shifts in H₂ 1–0 S(1) between symmetric positions on either side of the jet axis, after averaging across 3 slicing mirrors with $-0'.4 \leq \Delta Y \leq -0'.2$. The 1σ error bars include the fitting error due to noise and the 1 km s^{−1} rms instrumental drifts from spaxel to spaxel. Blue lines illustrate the typical range of spurious instrumental velocity gradients along slicing mirrors, as measured from OH lines (see Sect. 2). Residual errors in absolute calibration and correction for uneven-slit illumination cancel out here.

to search for transverse velocity gradients possibly indicative of rotation in the wide-angle H₂ lobe.

The differences in centroid velocity of H₂ 1–0 S(1) between symmetric positions across the jet axis are represented in Fig. 6. Note that any residual errors in absolute calibration and uneven-slit illumination correction cancel out (the illumination is symmetric with respect to the jet axis, to first order). To increase S/N, we averaged the 3 slicing mirrors centered at distances ΔY between $\approx 0'.2$ and $\approx 0'.4$ from the star, where H₂ emission is broadest. We then determined the velocity centroid by Gaussian fitting at each offset ΔX across the axis (keeping the original spaxel sampling of 0′.05 in this direction). In exposure 2, spaxels are not positioned symmetrically on either side of the jet axis, therefore centroid velocities at ΔX < 0 were linearly interpolated at positions symmetric from those at ΔX > 0 before computing velocity differences. Individual results from the two exposures are shown in Fig. 6. Blue lines superposed in Fig. 6 illustrate the expected range of spurious velocity shifts due to instrumental effects along slicing mirrors (“slope effects”, see Sect. 2).

When taken individually, all velocity differences plotted in Fig. 6 are compatible with zero to within their respective error bars, except in exposure 1 at $\pm 0'.1$ from the axis. However, there is a systematic consistent trend at most positions and in both exposures for spectra at positive ΔX (SE) to be more blueshifted than those at negative ΔX (NW). This would correspond to rotation in the same sense as the CO disc and optical jet in DG Tau (Testi et al. 2002; Bacciotti et al. 2002; Coffey et al. 2007). Unfortunately, the observed trends are also of the same order as the maximum residual instrumental slope along slicing mirrors observed in OH sky lines (blue lines in Fig. 6). Although (i) most instrumental residual slopes are shallower than this; (ii) averaging over 3 slicing mirrors should decrease the effect; and (iii) there is only a 25% probability that it would go in the same sense as the observed gradient in both exposures, an instrumental origin cannot be totally excluded. Since we lack a bright OH sky exposure simultaneous with our data to correct for the effect

spaxel-by-spaxel, we can only put an upper limit on the true transverse velocity shifts in H₂ present in our data.

To obtain a conservative upper limit on the possible rotational shift at $\Delta X \pm 0''.2$ from the axis (where the H₂ rims peak, cf. Fig. 1), we take the average shift of the two exposures at this offset (-1.3 km s^{-1}), add its 3σ error bar (-4 km s^{-1}), and correct by the maximum expected instrumental effect in the opposite direction $\approx 2 \text{ km s}^{-1}$ (since this situation cannot be excluded either). We obtain an upper limit of $V_{\text{shift}} \leq 7 \text{ km s}^{-1}$ in the sense of disc rotation. In the ideal situation of a single flow streamline observed with infinite angular resolution, this would set an upper limit on the H₂ flow rotation speed of $V_\phi = V_{\text{shift}}/(2 \sin i) \leq 5 \text{ km s}^{-1}$ for a jet inclination to the line of sight of 40° . In reality, convolution by the PSF and contribution from several streamlines along the line of sight both act to reduce the observable velocity shifts (Pesenti et al. 2004), and the true V_ϕ could be somewhat higher than this.

3.3. H₂ temperature, column and volume densities, and emitting area

Beck et al. (2008) computed the ratios of various ro-vibrational lines of H₂ towards the H₂ peak position, and found that they were compatible with a thermalized population at $T \approx 2000 \text{ K}$. To search for possible temperature gradients, we computed the 2–1 S(1)/1–0 S(0) ratio at several positions, after averaging over $0''.2$ along the jet and $0''.5$ across the jet to increase S/N in the fainter $v = 2-1$ line. We found a similar ratio at $\Delta Y = -0''.2$ and $-0''.4$ along the blue jet, of 0.07 ± 0.02 and 0.09 ± 0.02 respectively, consistent with the 0.07 ± 0.03 reported by Beck et al. (2008) towards the H₂ peak. Hence we assume a uniform temperature $T \approx 2000 \text{ K}$ in the following. We note that the 1–0 S(0)/1–0 S(1) ratio $\approx 0.25 \pm 0.03$ observed towards the H₂ peak (Takami et al. 2004; Beck et al. 2008; Greene et al. 2010) combined with Eq. (5) of Kristensen et al. (2007) indicates an H₂ ortho/para ratio ≈ 3 consistent with the LTE value. We assume the same holds throughout the region.

Our flux-calibrated data in H₂ 1–0 S(1) can be converted into column densities in the upper level of the transition ($v = 1, J = 3$) through $N_{1,3} = F_{1-0S(1)} \times (4\pi)/(h\nu_{ul}A_{ul}) = 3.8 \times 10^{19} \text{ cm}^{-2} \times F_{1-0S(1)} (\text{erg s}^{-1} \text{ cm}^{-2} \text{ sr}^{-1})$. Assuming LTE at 2000 K and an ortho/para ratio of 3, the total column density of hot H₂ gas is then given by $N_{\text{H}_2} = N_{1,3}/1.28 \times 10^{-2}$ (Takami et al. 2004). The inferred column density of hot H₂ reaches $4 \times 10^{19} \text{ cm}^{-2}$ towards the H₂ peak at $-0''.1$ from the star (peak brightness $\approx 0.013 \text{ erg s}^{-1} \text{ cm}^{-2} \text{ sr}^{-1}$; cf. Fig. 2), while the typical value at the center of the blue lobe is $\approx 10^{19} \text{ cm}^{-2}$ (central brightness $\langle F_{1-0S(1)} \rangle \approx 3 \times 10^{-3} \text{ erg s}^{-1} \text{ cm}^{-2} \text{ sr}^{-1}$; cf. Fig. 2). Since the inner peak might have a contribution from an axial jet knot (see FUV image of Schneider et al. 2013a), and the rims are clearly limb-brightened, we consider the brightness towards the blue lobe center as our best estimate for the intrinsic “face-on” column density of the layer producing the wide-angle H₂ emission. Both our image and that of Schneider et al. (2013a) suggest that the rims are thinner than $0''.1 = 14 \text{ AU}$, yielding a lower limit to the volume density of hot H₂ in the emitting layer of $n_{\text{H}_2} \geq 5 \times 10^4 \text{ cm}^{-3}$.

The top panels of Fig. 4 plot the 1–0 S(1) luminosity *per* $0''.1$ length along the jet, integrated over a full width of $1''$ across the jet, for each individual exposure. Even though the H₂ emission is narrowest at the base and widens out, the luminosity still peaks at $-0''.1$ and then decreases gradually with distance. The total luminosity integrated over the whole emitting

region is $L_{1-0S(1)} = 1.9 \times 10^{-5} L_\odot$, only 50% more than in the $0''.3$ -wide slit of Takami et al. (2004). The total mass of hot H₂ at 2000 K, assuming LTE, is then $3 \times 10^{-8} M_\odot$, while the characteristic emitting area at average brightness level is $A \approx L_{1-0S(1)}/(4\pi \langle F_{1-0S(1)} \rangle) = 2 \times 10^{30} \text{ cm}^2 \approx (90 \text{ AU})^2$.

We note that we do not include any correction for dust attenuation of the H₂ 1–0 S(1) line fluxes. Although Beck et al. (2008) derived a rather high $A_V = 11.2 \pm 10 \text{ mag}$ towards the H₂ peak, the uncertainty in their estimate is large, due to strong telluric absorption in H₂ Q-branch lines near $2.4 \mu\text{m}$. Furthermore, the optical jet brightness keeps increasing all the way up to $0''.1$ from the star (Bacciotti et al. 2000), suggesting that the atomic jet suffers only moderate circumstellar dust extinction. Hence, any 11 mag obscuring layer would have to lie behind the blue atomic jet lobe yet in front of the blueshifted H₂ peak, which seems very contrived. Finally, the strikingly similar morphology of FUV H₂ emission imaged by Schneider et al. (2013a) to that seen in the near-infrared 1–0 S(1) line also argues strongly for a low A_V to the hot H₂. We thus assume that dust obscuration is negligible in *K*-band lines.

4. Origin of the wide-angle H₂ emission in DG Tau

In this section, we re-examine possible origins for the wide-angle, limb-brightened H₂ 1–0 S(1) emission in the blue lobe of DG Tau, taking into account the new information extracted from our SINFONI data on the geometry, proper motion, radial velocities, and surface brightnesses (cf. previous section). In Sect. 4.1, we determine the allowed shock parameter space able to explain both the 1–0 S(1) surface brightness and the 2–1 S(1)/1–0 S(1) line ratio. In Sect. 4.2, we model geometrical and projection effects to constrain the velocity field compatible with the observed radial velocities. Finally, we combine these two sets of constraints to examine the plausibility and requirements of several scenarios proposed for the origin of wide-angle H₂ in DG Tau and similar sources (e.g., HL Tau):

- an irradiated disc atmosphere/envelope;
- a molecular MHD disc wind heated by ambipolar diffusion;
- a forward shock driven into the disc/envelope;
- a reverse shock driven back into a molecular wide-angle wind.

4.1. Allowed shock parameter space

Beck et al. (2008) compared the H₂ line ratios in DG Tau with planar shock models from Smith (1995) with preshock density $2 \times 10^6 \text{ cm}^{-3}$. They mention good agreement with both an 8 km s^{-1} non-dissociative J(ump)-type shock, and a 35 km s^{-1} multifluid C(ontinuous)-type shock (where ions and neutrals are decoupled). We here use the additional constraint provided by the calibrated 1–0 S(1) H₂ surface brightness, together with a larger grid of planar shocks computed by Kristensen et al. (2008), to explore more extensively the shock parameter space that could reproduce the DG Tau observations.

The predicted H₂ surface brightnesses depend on three parameters: the shock velocity V_s , the preshock hydrogen nucleus density, n_{H} , and the dimensionless magnetic field parameter³ $b \equiv B(\mu\text{G})/\sqrt{n_{\text{H}}(\text{cm}^{-3})}$, where B is the magnetic field component parallel to the shock front. The grid includes both single-fluid J-type shocks with $b = 0.1$, and steady multifluid C-type

³ This parameter is related to the Alfvén speed in the preshock gas through $V_A = b \times 1.88 \text{ km s}^{-1}$.

shocks with b ranging from 0.5 to 10. Preshock densities range from 10^4 to 10^7 cm⁻³. The preshock gas is assumed fully molecular with no UV field and a standard ISM dust content and cosmic ray flux; the latter determines in particular the initial abundances of charged species and atomic H.

We note that model predictions assume a face-on view. A sideways view would increase the observed surface brightness by a factor $1/\cos(i)$ for an infinite slab. This effect does not introduce large errors when fitting H₂ emission near the head of a bowshock, where the path-length is limited by the strong curvature (Gustafsson et al. 2010), but will be more severe for a tilted cavity where the front side is almost entirely tangent to the line of sight, as suggested here by the brighter rim towards the star (see Sect. 4.2). Hence, we will rather compare the face-on shock predictions with the 1–0 S(1) surface brightness towards the center of the H₂ cavity, where limb-brightening effects will be minimal.

In Fig. 7 we compare the observed 1–0 S(1) surface brightness and 2–1 S(1)/1–0 S(1) ratio with model predictions for J-shocks with $b = 0.1$ (top panel) and C-shocks with $b = 1$ (bottom panel). It may be seen that the 2–1 S(1)/1–0 S(1) ratio is much more sensitive to V_s than to n_H , with changes of a factor 2 in the former having a stronger effect on the ratio than a change of a factor 10 in the latter. In the case of J-shocks, the data point towards the cavity center is fitted with a high $n_H \approx 10^6$ cm⁻³ and a low shock speed $V_s \approx 9$ – 10 km s⁻¹. In the case of C-shocks with $b = 1$, the models point to a lower density $n_H \approx 10^4$ cm⁻³ and a higher shock speed $V_s \approx 52$ km s⁻¹. Similar plots for C-shocks with $b = 0.5$ and $b = 10$ are shown in Appendix B. The data point for the inner peak at $-0'.1$ from the star (top triangular symbol in Fig. 7) would require a roughly 10 times higher preshock density than the central point. However the required shock speed would change by less than a factor 2. Therefore, our conclusions on V_s are robust even if the surface brightness at the cavity center is affected by residual geometric projection effects.

Table 1 summarizes the pairs of values (n_H , V_s) compatible with observations for each magnetic field parameter b . It may be seen that a larger magnetic parameter b requires higher shock speed and lower density to match the observations. It is noteworthy that in all cases, the allowed range of shock speed reproducing the observed 2–1 S(1)/1–0 S(1) ratio is very narrow, setting strong constraints on scenarios of shock-heating. For each planar shock model able to reproduce the H₂ 1–0 S(1) brightness and 2–1/1–0 ratio, we also calculated $V_n(\text{H}_2)$, the (emission-weighted) centroid velocity of the H₂ 1–0 S(1) emission layer in the reference frame of the shock wave. In J-shocks, where deceleration is almost instantaneous, $V_n(\text{H}_2)$ is essentially zero. In contrast, we find that it is typically $\approx 60\%$ of the shock speed in the C-shocks of Table 1, where deceleration of the neutrals occurs through collisions with the (rare) ions and is therefore much more gradual.

4.2. Constraints on the intrinsic velocity field of the wide-angle H₂

The limb-brightened morphology of the wide-angle H₂ emission is suggestive of a tilted cavity. Hence, observed radial velocities are affected by complex projection effects. We thus need 3D geometrical models to infer the true velocity field of the H₂ emitting gas parallel (V_{\parallel}) and perpendicular (V_{\perp}) to the cavity surface. To remain as general as possible, we consider two basic toy models: (1) a hollow cone with its apex at the source position and its axis aligned with the blue jet; and (2) a (half or full) hollow sphere centered at a projected distance z_{proj} from the source

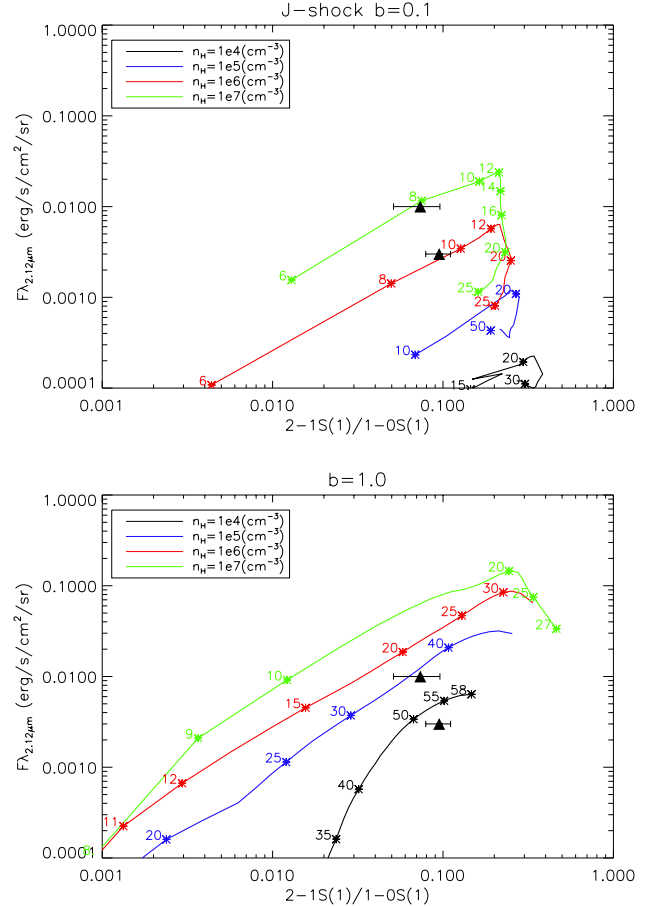


Fig. 7. H₂ surface brightness in the 1–0 S(1) line against the $v = 2$ –1 S(1)/ $v = 1$ –0 S(1) ratio as observed in the DG Tau blue lobe (lower triangle: center of blue lobe, upper triangle: inner peak) and as predicted for planar shock models viewed face-on from Kristensen et al. (2008) (colour curves). The error bars on observed surface brightness are smaller than the symbol size, while the difference between the two symbols illustrates the maximum uncertainty due to projection/limb-brightening effects. *Top panel:* planar J-shocks with $b = 0.1$. *Bottom panel:* C-shocks with $b = 1$. Each model curve corresponds to a different value of the preshock hydrogen nucleus density n_H , increasing from bottom to top. The shock speed V_s increases to the right and some values are marked along the curves to guide the eye. Similar plots for C-shocks with $b = 0.5$ and $b = 10$ are shown in Appendix B. Note the narrow range of shock speeds reproducing the observed 2–1 S(1)/1–0 S(1) ratios.

along the blue jet axis. They are assumed infinitely thin and with uniform surface brightness. We built synthetic 3D datacubes for several inclinations to the line of sight. Each channel map is convolved by a Gaussian PSF of FWHM $0'.12$, and the PSF of the spectrum at (0, 0) is subtracted out (as performed in our observations for the purpose of telluric and continuum subtraction, see Sect. 2). Residual emission maps are then built and compared by eye with the deconvolved image of Fig. 1, to determine the geometrical parameters reproducing the H₂ cavity shape, size, and limb-brightened appearance.

In the case of cones, the deconvolved map is best reproduced with a spherical radius $R_{\text{max}} \approx 0'.43$ (60 AU) and half-opening angle $\theta = 30^\circ \pm 3^\circ$ for inclinations $i = 45^\circ \pm 5^\circ$ to the line of sight. A typical predicted map for $\theta = 27^\circ$ and $i = 40^\circ$ is shown in the top panel of Fig. 8, superposed on the observed deconvolved map. The front side of the cavity is almost tangent to the line of sight, so that the limb-brightened rim gets brighter

Table 1. Planar shock parameters for the peak and central positions in the H₂ cavity, assuming a face-on view.

$b = B(\mu\text{G})/\sqrt{n_{\text{H}}(\text{cm}^{-3})}$		J-shock	C-shocks						
		0.1	0.5	1.0	2.0	3.0	4.0	5.0	10.0
Peak	$n_{\text{H}} (\text{cm}^{-3})$	10^7	$10^5\text{--}10^6$	$5 \times 10^4\text{--}10^5$	$\sim 4 \times 10^4$	$\sim 3 \times 10^4$	$\sim 3 \times 10^4$	$\sim 2 \times 10^4$	10^4
	$V_{\text{s}} (\text{km s}^{-1})$	8	32–16	41–35	~ 50	~ 59	~ 65	~ 70	88
Center	$n_{\text{H}} (\text{cm}^{-3})$	10^6	$\approx 5 \times 10^4$	$\approx 10^4$	$\leq 10^4$	$\leq 10^4$	$\leq 10^4$	$\leq 10^4$	$< 10^4$
	$V_{\text{s}} (\text{km s}^{-1})$	9–10	≈ 30	52	≥ 60	≥ 65	≥ 70	≥ 75	> 90

closer to the star, as observed; the narrow peak observed at $-0''.1$ is not fully reproduced, and may include contribution from a jet knot. The cone surface is $(75 \text{ AU})^2$, in good agreement with the full emission surface $\approx (90 \text{ AU})^2$ estimated in Sect. 3.3.

In the case of a sphere, the best fit to the overall size and shape is for a radius $R_{\text{max}} \approx 0''.2$ (28 AU) centered at $z_{\text{proj}} \approx 0''.28$ (40 AU) along the blue jet. However, to obtain a brighter rim at the base, the emissivity must be strongly enhanced in the hemisphere facing the star. After convolution by our PSF, the map and centroid velocities are then undistinguishable from those predicted for that single hemisphere. For simplicity, we thus consider a half-sphere in the following. The predicted map is compared with the observed one in the bottom panel of Fig. 8. The emission surface of $(70 \text{ AU})^2$ is close to that of the cone model.

For each geometry that reasonably reproduces the H₂ 1–0 S(1) image, we then construct a synthetic PV diagram along the jet axis, after convolving the datacube spatially by a Moffat function (a good fit to the raw PSF delivered by our AO system) and spectrally by a Gaussian of FWHM 88 km s^{-1} (median resolution of SINFONI over the field of view). We then compute velocity centroids and line widths as a function of distance in the same way as for our Fig. 4, i.e., by performing a Gaussian fit to each PV spectrum. We find that the broad wings of the Moffat function severely smear out velocity gradients. Spatial convolution by the PSF is thus essential for a meaningful comparison with observed centroids. In contrast, spectral convolution affects only the line widths. For simplicity, velocity vectors are assumed to have a constant modulus V_0 and to make a constant angle α from the local normal to the cavity. The flow velocity parallel and perpendicular to the cavity wall are given by $V_{\parallel} \equiv V_0 \sin \alpha$ and $V_{\perp} \equiv V_0 \cos \alpha$, counted positively away from the star.

The predicted PV centroid velocities in units of V_0 are plotted in the top panel of Fig. 9 as a function of distance along the jet, for both the cone and the half-sphere models presented in Fig. 8. The results are strikingly similar despite the different geometries. This gives us confidence that the derived conclusions are robust and not dependent on the exact cavity shape. For a pure parallel flow oriented away from the source ($\cos \alpha = 0$), the PV centroid is blueshifted at all distances by $\approx -0.5V_{\parallel}$. In contrast, for a pure perpendicular flow oriented outward ($\cos \alpha = 1$), the centroid is everywhere redshifted by an amount that increases with distance up to $\approx +0.65V_{\perp}$. Centroids for intermediate values of $\cos \alpha$ are simply given by a linear combination of these two extremes. A particularly interesting case is $\cos \alpha = 0.6$ (i.e., $V_{\parallel}/V_{\perp} = 1.3$), shown by the middle curves in Fig. 9. This produces radial velocities that drop to essentially zero at $-0''.4$ from the star, as observed.

In the bottom panel of Fig. 9, the observed H₂ 1–0 S(1) centroids in a PV along the jet (from Fig. 4) are compared with those predicted for a conical surface (similar conclusions would be reached for the half-sphere). Only an intermediate value of $\cos \alpha \approx 0.6$ (i.e., $V_{\parallel}/V_{\perp} = 1.3$) can reproduce at the same time the large blueshift observed at $-0''.1$, and the centroids close to

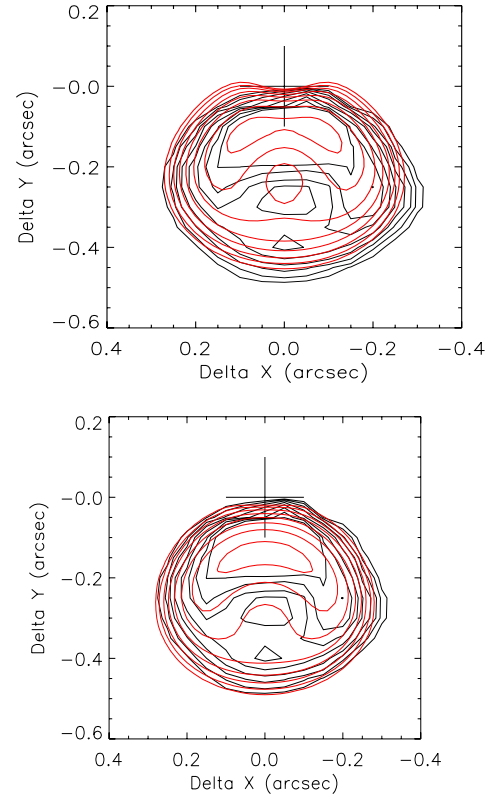


Fig. 8. Predicted emission maps for toy models (black contours) convolved by a Gaussian of $0''.12$ FWHM, superimposed on the observed deconvolved H₂ 1–0 S(1) map from Fig. 1 (red contours). *Top:* hollow cone viewed 40° from pole-on with radius 60 AU and semi-opening angle 27° . *Bottom:* hollow half-sphere viewed 45° from pole-on, with radius 28 AU and center projected at 40 AU along the blue jet. All contours increase by factors of $\sqrt{2}$. The PSF of the spectrum at (0, 0) was subtracted in all cases.

zero observed at $-0''.4$. In this case, the data are well fitted with $V_{\perp} \approx 20 \text{ km s}^{-1}$. A larger $V_{\perp} \approx 30 \text{ km s}^{-1}$ would predict excessive blueshifts close to the source. Examination of the predicted line widths yields the same result, namely that $V_{\perp} \approx 20 \text{ km s}^{-1}$ is compatible with the data while $V_{\perp} \approx 30 \text{ km s}^{-1}$ predicts excessive line broadening. The maximum flow speed compatible with the observed radial velocities and line widths is thus $V_0 = V_{\perp}/\cos \alpha \approx 30 \text{ km s}^{-1}$.

If the -20 km s^{-1} blueshift at $-0''.1$ is instead due to an axial jet knot, the value of α in the wide-angled rims is no longer well determined. The only constraint now is that PV centroids at $-0''.2$ to $-0''.4$ fall in the range -5 to 0 km s^{-1} (within the uncertainties discussed in Sect. 2). This approximately translates into the condition $(V_{\parallel} - V_{\perp}) \approx 5 \text{ km s}^{-1}$. For example, a pure inward perpendicular flow with $V_{\perp} \approx -5 \text{ km s}^{-1}$ (dash-dotted curve in the bottom panel of Fig. 9) or a pure parallel flow with

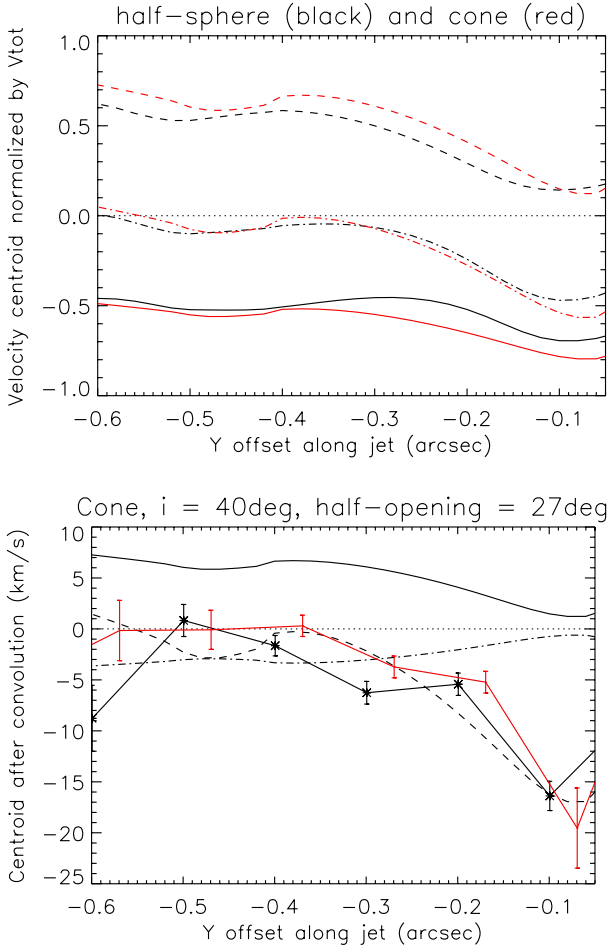


Fig. 9. *Top panel:* predicted centroid velocities in units of the total gas speed for a PV along the jet, for the same two models shown in Fig. 8: cone (in red) and half-sphere (in black). The bottom solid curves are for a pure outward parallel flow ($\cos \alpha = 0$), top curves for a pure outward perpendicular flow ($\cos \alpha = 1$), and middle curves for an intermediate situation ($V_{\parallel}/V_{\perp} = 1.3$, $\cos \alpha = 0.6$). *Bottom panel:* observed H₂ 1–0 S(1) centroid velocities in a PV along the jet axis (symbols with error bars, from Fig. 4) compared with predictions for the conical model. Dashed curve: $V_{\perp} = 20 \text{ km s}^{-1}$ and $\cos \alpha = 0.6$; dash-dotted curve: $V_{\perp} = -5 \text{ km s}^{-1}$ and $V_{\parallel} = 0$; solid curve: $V_{\perp} = +10 \text{ km s}^{-1}$ and $V_{\parallel} = 0$.

$V_{\parallel} \approx 5 \text{ km s}^{-1}$ (not shown) become compatible with observations within the uncertainties.

In summary, the observed radial velocities of H₂ 1–0 S(1) in the PV diagram limit the gas motion perpendicular to the cavity walls to $-5 \geq V_{\perp} \leq +5 \text{ km s}^{-1}$, unless there is a significant parallel component $V_{\parallel} \approx 1.3V_{\perp}$ in which case V_{\perp} can be up to 20 km s^{-1} and the total flow speed can reach 30 km s^{-1} . The above constraints help to narrow-down the possible wind and ambient properties in various scenarios, which we now examine.

4.3. Irradiated disc atmosphere

We first reconsider the scenario depicted in panel a of Fig. 10, where rovibrational H₂ emission in DG Tau traces a disc atmosphere heated by stellar FUV and X-ray radiation. Indeed, a recent indication that the warm H₂ emitting in 1–0 S(1) is strongly irradiated is the presence of Ly α -pumped H₂ FUV emission with the same 2D emission morphology as in 1–0 S(1) (Schneider et al. 2013a) and with relative intensities among pumping levels

indicating a similar gas temperature $\approx 2500 \text{ K}$ (Herczeg et al. 2006).

Beck et al. (2008) previously argued against stellar FUV-X-ray photons as the dominant heating source for the extended ($\geq 100 \text{ AU}$) H₂ emission around CTTS, including DG Tau, based on the irradiated disc models of Nomura & Millar (2005) and Nomura et al. (2007) which predict surface temperatures less than 2000 K beyond disc radii of 20 AU . However, we note that the FUV stellar flux in DG Tau is higher than adopted in these models. The extinction-corrected FUV excess in DG Tau is flat over at $1400\text{--}2000 \text{ \AA}$, with a flux measured on earth of $2 \times 10^{-13} \text{ erg s}^{-1} \text{ cm}^{-2} \text{ \AA}^{-1}$ (Gullbring et al. 2000). This corresponds to a normalized FUV flux⁴ $G_0 = 5 \times 10^5$ at a distance of $0''.1 = 14 \text{ AU}$ from the star, 5 times more than in the model of Nomura et al. (2007). With this G_0 value, the PDR models of Le Petit et al. (2006) predict H₂ line ratios compatible with observations for $n_{\text{H}} = 10^6\text{--}10^7 \text{ cm}^{-3}$, although the predicted 1–0 S(1) brightness for a face-on view is 4–14 times lower than observed. Towards the center of the H₂ cavity at $0''.25 = 35 \text{ AU}$, the unattenuated FUV field is $G_0 = 8 \times 10^4$ and the predicted brightness for $n_{\text{H}} = 10^6\text{--}10^7 \text{ cm}^{-3}$ is now only 2–5 times lower than observed, although the predicted 2–1 S(1)/1–0 S(1) ratio $\approx 0.15\text{--}0.2$ is slightly too high. Given that PDR models apply only to infinite uniform slabs, and necessarily involve some uncertainties, this may still be considered as promising agreement. Recently, Schneider et al. (2013a) argued that FUV pumping of H₂ in the region $0''.2\text{--}0''.4$ from DG Tau may be enhanced by Ly α photons from the $30\text{--}100 \text{ km s}^{-1}$ atomic shocks known to be present in the DG Tau jet. If the Ly α pumping flux that they infer is uniformly spread over the emission area $\approx 2 \times 10^{30} \text{ cm}^2$ estimated here (see Sect. 3.3), then $G_0 \approx 10^6$. This enhanced level of irradiation could reproduce *both* the face-on cavity brightness in 1–0 S(1) and the 2–1 S(1)/1–0 S(1) ratio if $n_{\text{H}} = 10^7 \text{ cm}^{-3}$ (Le Petit et al. 2006), without the need for shock excitation.

Assuming that the warm wide-angle H₂ in DG Tau traces the 2000 K layer in the irradiated disc atmosphere, a photoevaporative flow would seem a natural hypothesis to explain the observed slight blueshifts. Photo-evaporation occurs mostly outside of a disc radius $r_{\text{cr}} \approx 0.15r_{\text{g}}$, where r_{g} is the radius where the sound speed equals the keplerian speed (Dullemond et al. 2007). For the mass of DG Tau $\approx 0.7 M_{\odot}$ and an assumed temperature of 2000 K at the flow base, we obtain $r_{\text{cr}} = 10(\mu/2) \text{ AU}$ with μ the mean molecular mass; A higher initial temperature will give a smaller r_{cr} . This is consistent with the maximum radius $\approx 0''.1 = 14 \text{ AU}$ at the base of the H₂ rims in the FUV image of Schneider et al. (2013a). Hydrodynamical models (e.g., Font et al. 2004) predict that the expected evaporation speed is on the order of a few times the sound speed $c_s = 3(T/2000 \text{ K}) \text{ km s}^{-1}$ for molecular gas. The dot-dashed curve in Fig. 9 shows the predicted PV centroids for a photoevaporative flow directed into the cavity at 1.5 times the sound speed ($V_{\perp} = -5 \text{ km s}^{-1}$); the predicted low blueshifts are roughly consistent with observed centroids beyond $0''.2$ from the source; the high blueshifts of -20 km s^{-1} closer to the star would then trace a faster axial jet knot of different origin.

Takami et al. (2004) ruled out FUV-Xray irradiation as the excitation mechanism of the warm blueshifted H₂ in DG Tau, because they inferred a momentum flux of $6.5 \times 10^{-6} M_{\odot} \text{ km s}^{-1} \text{ yr}^{-1}$ too large compared to typical values in CO outflows from low-luminosity Class I protostars. The large

⁴ Defined as the average ratio over $910\text{--}2066 \text{ \AA}$ of the incident FUV field to the standard interstellar field (see e.g., Tielens & Hollenbach 1985).

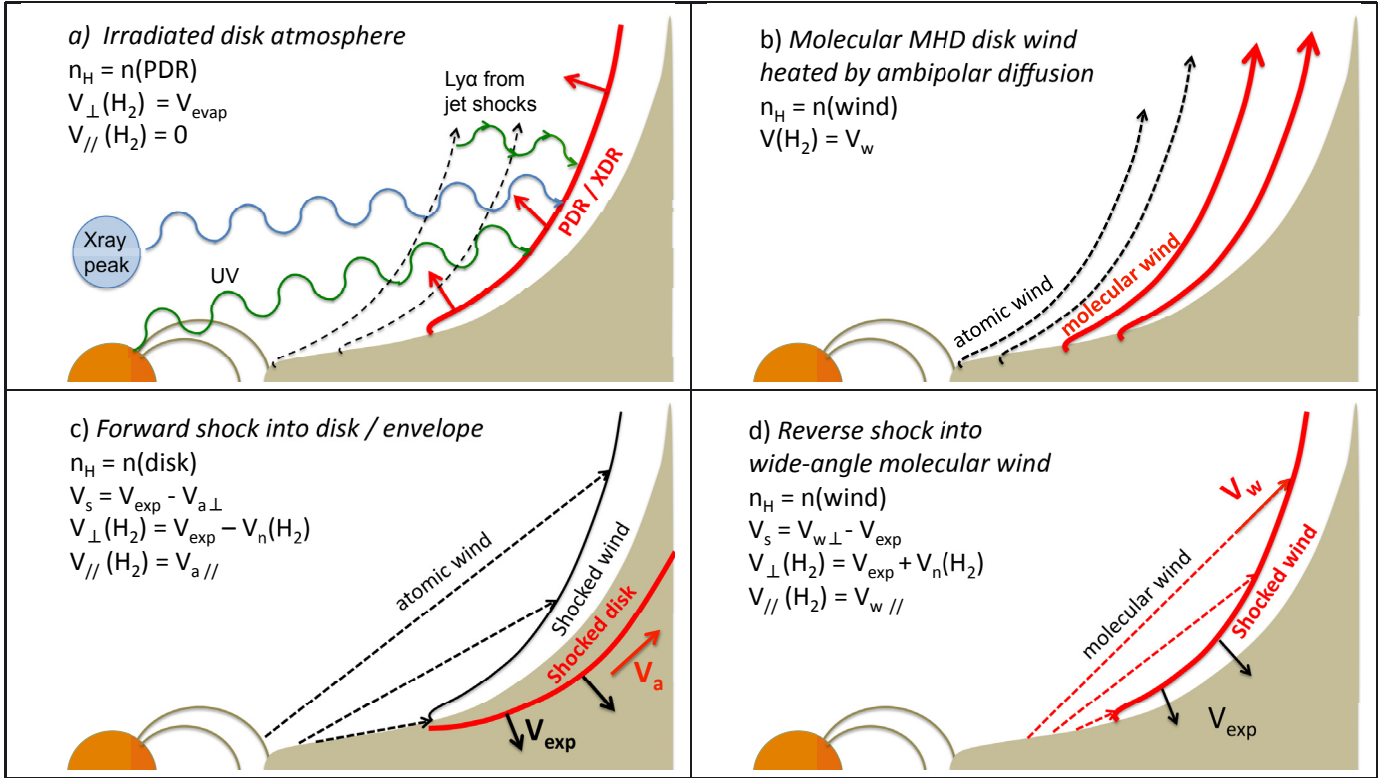


Fig. 10. Schematic representation of the 4 scenarii discussed for the origin of the wide-angle rovibrational H_2 emission in DG Tau. The layer of emitting H_2 at 2000 K is drawn in solid red. Wide-angle wind streamlines are shown as dashed (black if atomic, red if molecular) lines. The velocity of the emitting gas perpendicular and parallel to the cavity wall (V_{\perp} and V_{\parallel}), and the shock speed V_{s} and preshock density n_{H} when applicable, are also listed as a function of the expansion proper motion of the cavity V_{exp} , the velocity of the H_2 1–0 S(1) emitting layer in the frame of the shock wave, $V_{\text{n}}(\text{H}_2)$, and the initial velocity of the ambient gas (V_{a}) or molecular wind (V_{w}).

momentum flux of Takami et al. (2004) stems from an assumed mean flow speed $\approx 20 \text{ km s}^{-1}$, length along the flow $\approx 40 \text{ AU}$, emitting area of $4 \times 10^{30} \text{ cm}^2$, and a large total column density $N_{\text{H}} = 10^{21} \text{ cm}^{-2}$ (the gas at 2000 K in equilibrium PDRs has a low molecular abundance $\approx 10^{-3}$ – 10^{-2} ; Burton et al. 1990). On the other hand, with our twice smaller characteristic emitting area, and longer spatial extent of 60 AU along the jet axis, the momentum flux would become only $2 \times 10^{-6} M_{\odot} \text{ km s}^{-1} \text{ yr}^{-1}$, comparable to CO outflows in Class I sources of $1 L_{\odot}$ (Bontemps et al. 1996). In addition, most of the warm H_2 at wide angle could be photoevaporating at low speed $\leq 5 \text{ km s}^{-1}$ (see above), giving an even lower momentum flux by a factor 4. Since DG Tau is a “flat spectrum” TTS at the border between Class I and Class II, this would not be prohibitive anymore. Furthermore, we caution that momentum fluxes in Class I outflows are based on CO observations in low-J lines with a large beam ($\geq 10''$ typically) and a bias towards cold gas at $T \leq 100 \text{ K}$. They may not be sensitive to the warm and compact outflows at 2000 K on $< 100 \text{ AU}$ scales probed by H_2 imaging. Rovibrational CO lines would be a better tracer of such conditions, and recent CO $v = 1-0$ observations at high resolution do provide evidence for warm, compact, and slow molecular winds towards several high-accretion Class II sources, attributed to disc photoevaporation (Bast et al. 2011). The corresponding momentum fluxes are not known sufficiently well yet to compare with DG Tau.

We conclude that FUV irradiation does not seem fully excluded as the heating and perhaps acceleration mechanism of the warm H_2 wide-angle cavity in DG Tau. However, an important open issue with this scenario is the high PDR density of $n_{\text{H}} = 10^7 \text{ cm}^{-3}$ needed to reproduce the observed brightness

and line ratios. At radii of 10–30 AU, static models of the irradiated disc in DG Tau reach this density only at polar angles $\theta \approx 60^\circ$ (Podio et al. 2013), whereas toy models reproducing the observed morphology favor a layer much higher up from the midplane, at $\theta \approx 30 - 45^\circ$ (see Sect. 4.2). Lower densities might be possible if the PDR is not at equilibrium, e.g., if the FUV flux was only recently “turned-on” (Hollenbach & Natta 1995) or if photoevaporation constantly exposes fresh H_2 to the FUV flux. However, the observed limit on the rim thickness ≤ 0.1 combined with the typical gas column at 2000 K in PDRs of $N_{\text{H}} \approx 10^{21} \text{ cm}^{-2}$ still points to a high $n_{\text{H}} \geq 5 \times 10^6 \text{ cm}^{-3}$. Time-dependent hydro-chemical models of disc PDRs including photoevaporation and irradiation by $\text{Ly}\alpha$ photons from jet shocks would be in order to definitely test this scenario.

4.4. Molecular MHD disc wind heated by ambipolar diffusion

Based on the pioneering work of Safier (1993), Takami et al. (2004) was first to suggest that the wide-angle slow H_2 emission in DG Tau might trace the outer molecular streamlines of an MHD disc wind heated by ambipolar diffusion, whose inner atomic streamlines would produce the faster and more collimated emission seen in optical lines. This scenario is depicted in panel b of Fig. 10.

Panoglou et al. (2012) recently carried out a thorough study of the thermal and chemical structure of a steady, self-similar MHD disc wind solution from Casse & Ferreira (2000), with a lever arm parameter $\lambda = 13$ selected to provide a good fit to the tentative rotation signatures in the atomic jet of DG Tau (Pesenti et al. 2004). For an accretion rate $\dot{M}_{\text{acc}} \sim 10^{-6}$ – $10^{-7} M_{\odot} \text{ yr}^{-1}$,

Panoglou et al. find that H₂ molecules can survive against both collisional dissociation and photodissociation by the stellar FUV and X-ray photons when launched from disc radii greater than about 1 AU. Heating by ambipolar diffusion then creates a temperature plateau of 2000–4000 K over 10–100 AU scales, in good agreement with the observed uniform H₂ temperature in DG Tau (see Sect. 3.3). For a launch radius $r_0 \approx 10$ AU, compatible with the rim radius at the base of the blue lobe, this particular MHD disc wind solution predicts that the streamline will reach a radius ≈ 50 AU at an altitude of 50 AU above the disc (see Fig. 1 of Panoglou et al. 2012), similar to the measured maximum FWHM of the H₂ cavity at the corresponding projected distance (see Fig. 2). The predicted rotation speed is $V_\phi \approx 5$ km s⁻¹, compatible with our upper limit on transverse rotation signatures (see Sect. 3.2.3). At the same position, the streamline reaches a poloidal flow velocity $V_0 \sim 15$ km s⁻¹ consistent with the constraint $V_0 \leq 30$ km s⁻¹ from modeling of radial velocities (see Sect. 4.2).

Assuming that the wide-angle H₂ emission does trace a fully molecular MHD disc wind uniformly heated to 2000 K by ambipolar diffusion, the one-sided wind mass flux may be calculated following the method of Takami et al. (2004), assuming LTE. Our toy models favor a slightly larger spatial scale along the jet axis $R_{\max} \approx 60$ AU, giving $\dot{M}_w \sim 10^{-9} M_\odot \text{ yr}^{-1}$. With an estimated accretion rate of $\dot{M}_{\text{acc}} = (3 \pm 2) \times 10^{-7} M_\odot \text{ yr}^{-1}$ over the period 1996–2005 (Agra-Amboage et al. 2011), the ejection-accretion ratio in the blue lobe of the molecular wind would thus be ≈ 0.003 – 0.014 . This would be consistent with the lever arm parameter $\lambda = 13$ of the MHD disc wind solution if the external launch radius, r_e , and internal launch radius, r_i , for the molecular streamlines are in a ratio $r_e/r_i \approx 1.15$ – 2 (see, e.g., Eq. (17) of Ferreira et al. (2006)). The corresponding width of the flow would be 50–13% of the cavity radius, compatible with observations. We infer $r_i \approx 5$ – 8 AU for $r_e \approx 10$ AU. This value of r_i matches rather well with the outer launch radius ≈ 3 AU for the atomic LVC component inferred from rotation signatures (Pesenti et al. 2004).

Hence, the temperature, kinematics, morphology, and mass flux of the H₂ cavity in DG Tau all appear in promising agreement with a steady molecular MHD disc wind heated by ambipolar diffusion, ejected from 5–10 AU. However, calculations of beam-convolved synthetic H₂ images and PV diagrams of MHD disc winds taking into account non-LTE effects, the full 3D velocity field, and a range of streamlines are necessary to test this scenario. Such detailed work is beyond the scope of the present paper and will be the subject of future work.

4.5. Forward shock driven into the environment

In this scenario, depicted in panel c) of Fig. 10, the observed wide-angle H₂ emission traces ambient gas from the surrounding disc/envelope, that is, being shocked and swept-up into a shell by the wide-angle atomic wind. This scenario is traditionally invoked to explain CO molecular outflow cavities seen on larger scales around young protostars (Arce et al. 2007). It was proposed by Takami et al. (2007) to explain the small scale V-shaped biconical cavity of H₂ 1–0 S(1) emission around HL Tau, which bears strong resemblance to that in DG Tau; it is thus interesting to investigate whether the same scenario could apply to DG Tau itself. In the following discussion, we will neglect turbulent mixing along the cavity walls between the shocked ambient gas and the shocked wind. Current prescriptions for the entrainment efficiency, and numerical simulations

of wind-envelope interaction, both suggest that it would not be efficient on the scales of interest (Delamarter et al. 2000).

We place ourselves in the reference frame of the star, where we denote as V_{exp} the expansion proper motion of the shock wave into the envelope, and V_a the initial velocity of the ambient gas counted positively away from the star. We may then write the shock speed V_s suffered by ambient gas, and the velocity of post-shock warm H₂ perpendicular and parallel to the shock front, as

$$V_s = V_{\text{exp}} - V_{a\perp} \quad (1)$$

$$V_\perp = V_{\text{exp}} - V_n(\text{H}_2) = V_s + V_{a\perp} - V_n(\text{H}_2) \quad (2)$$

$$V_\parallel = V_{a\parallel}, \quad (3)$$

where $V_n(\text{H}_2) \geq 0$ is the centroid velocity of the shock-heated 1–0 S(1) emission layer in the reference frame of the shock wave (see Sect. 4.1).

Let us first consider the simplest case of a static ambient medium ($V_a = 0$), where the shock speed $V_s = V_{\text{exp}}$. Only a J-shock driven at $V_s = 10$ km s⁻¹ into a dense disc/envelope with $n_{\text{H}} \approx 10^6$ cm⁻³ and $b \leq 0.1$ can match at the same time the constraint from proper motions that $V_{\text{exp}} < 12$ km s⁻¹ (see Sect. 3.1) and the observed H₂ rovibrational excitation and brightness (see Table 1). Therefore, the cavity would have expanded to its observed half-width of $0'.2 = 30$ AU in only ≈ 15 years, meaning that it would trace a very recent wind “outburst”, even younger than in the case of HL Tau (70 years; Takami et al. 2007). Since it would be improbable to catch a rare event at such an early age, this phenomenon would have to be recurrent on timescales of a few decades, similar to the successive “bubbles” seen in XZ Tau (Krist et al. 2008).

However, a strong caveat with a shocked static preshock is that it predicts redshifted H₂ velocity centroids: in a J-shock, $V_n(\text{H}_2) \approx 0$, hence the shock-heated H₂ is moving perpendicular to the shock surface with $V_\perp = V_s \approx 10$ km s⁻¹ while $V_\parallel = 0$. The predicted centroids are plotted as a solid curve in the bottom panel of Fig. 9 for a conical toy model (similar results are obtained for a half-sphere). They are redshifted by $\approx +4$ to $+6$ km s⁻¹ at distances of $-0'.2$ to $-0'.4$ from the star, whereas observed centroids at the same distances are ≈ -5 to 0 km s⁻¹. The discrepancy is in the same sense in both exposures, and larger than our maximum possible residual errors in wavelength calibration and correction for uneven slit illumination (see Sect. 2). Therefore, a forward shock into a static ambient medium does not seem able to explain the observed centroids satisfactorily.

Let us now consider the case where ambient gas surrounding the cavity would be infalling towards DG Tau at speed V_{ff} (about 5 km s⁻¹ at a mean distance of 45 AU ($0'.3$) for a $0.7 M_\odot$ star). The V-shape of the cavity walls means that the infalling stream will have a very oblique incidence, with a dominant component parallel to the shock and directed towards the star. The terms $V_{a\perp} = -V_{\text{ff}\perp}$ and $V_{a\parallel} = -V_{\text{ff}\parallel}$ are then both negative, with the latter largely dominant. The effect on postshock centroids is to add a component with negative $V_0 = -V_{\text{ff}}$ and $\cos \alpha < 0.6$ ($V_{a\parallel}/V_{a\perp} > 1.3$). Figure 9 shows that this will produce additional redshift, worsening the discrepancy with observed centroids compared to the static ambient case. Therefore this scenario can be ruled out.

Let us now consider the opposite case where the ambient medium would be initially outflowing, and $V_{a\perp}$ and $V_{a\parallel}$ are both positive. To keep a shock speed $V_s \approx 10$ km s⁻¹ as required for H₂ excitation, the outflow perpendicular to the wall should be very slow at $V_{a\perp} = V_{\text{exp}} - V_s < 2$ km s⁻¹ (see Eq. (1)). Therefore V_\perp would remain essentially unchanged from the

static case, at 10–12 km s⁻¹ (see Eq. (2)). But redshifted centroids could be avoided if the (conserved) outflow parallel to the shock front $V_{\text{all}} = V_{\parallel}$ is about $1.3V_{\perp} \approx 13\text{--}15$ km s⁻¹ (see curve for $\cos \alpha = 0.6$ in Fig. 9, scaled to $V_0 \approx 17\text{--}20$ km s⁻¹). The mass flux in this preshock “ambient” outflow would be: $\mu m_{\text{H}} n_{\text{H}} V_{\text{all}} 2\pi r \Delta r = 2 \times 10^{-8} (2\Delta r/r)(r/30 \text{ AU})^2 M_{\odot} \text{ yr}^{-1}$. The origin of such a pre-existing massive molecular flow is an open issue. Previous ejecta from older outburst episodes would be expected to move mainly perpendicular to the shock surface, rather than parallel as needed to match the centroids. A photoevaporative flow from further out in the disc also seems difficult, as the column density of shocked gas swept up over 15 yr, $N_{\text{H}} = n_{\text{H}} V_{\text{s}} t = 5 \times 10^{20} \text{ cm}^{-2}$, would absorb a significant fraction of FUV photons before they reach the outer disc surface. A slow MHD-driven wind from the outer disc would remain an option; it is noteworthy that submm observations of CO and C⁺ towards DG Tau do show signs of slow expansion with a high-velocity tail reaching up to -10 km s⁻¹, albeit on scales of 5–10'' much larger than those probed here (Kitamura et al. 1996; Podio et al. 2013).

In summary, the detailed spatial, velocity, and brightness information extracted from our SINFONI data shows that a forward shock sweeping up ambient gas may explain the wide-angle H₂ 1–0 S(1) emission in DG Tau, but only under a set of restrictive circumstances: it should trace a very young (15 yr) swept-up shell expanding at $V_{\text{exp}} \approx 10\text{--}12$ km s⁻¹ into a pre-existing dense ($\approx 10^6 \text{ cm}^{-3}$) molecular wind moving mainly along the cavity walls at $\approx 13\text{--}15$ km s⁻¹. The origin of this preshock ambient outflow is an open issue. Accurate proper motion measurements of V_{exp} would provide a first crucial test of this scenario, and could also reveal deceleration indicative of an outburst origin, as well as possible recurrence.

4.6. Reverse shock into a wide-angle molecular wind

Beck et al. (2008) and Schneider et al. (2013a) proposed that the V-shaped H₂ emission in the blue lobe of DG Tau traces a “shocked molecular wide-angle wind” surrounding the atomic LVC. In panel d of Fig. 10, we illustrate the case where the “reverse” shock is driven into the molecular wind as it encounters the disc/envelope. Such a geometry is suggested by the smooth curved morphology of the emission (instead of a series of knots). The forward shock driven in the environment is assumed slow enough, or of low enough density, to have negligible emission in H₂ 1–0 S(1). The shock speed V_{s} and the postshock velocity of warm H₂ perpendicular and parallel to the shock front (again in the reference frame of the star) are now given as a function of the wind speed, V_{w} , by

$$V_{\text{s}} = V_{\text{w}\perp} - V_{\text{exp}} \quad (4)$$

$$V_{\perp} = V_{\text{exp}} + V_{\text{n}}(\text{H}_2) = V_{\text{s}} + V_{\text{w}\perp} + V_{\text{n}}(\text{H}_2) \quad (5)$$

$$V_{\parallel} = V_{\text{w}\parallel}. \quad (6)$$

Here, the constraint that $V_{\perp} \leq 20$ km s⁻¹ set by observed line centroids and line widths (see Sect. 4.2) imposes the same limit on $V_{\text{n}}(\text{H}_2)$. This is only fulfilled by J-shocks (where $V_{\text{n}}(\text{H}_2) \approx 0$) and by the C-shock with $b = 0.5$ in Table 1 (where $V_{\text{n}}(\text{H}_2) \approx 0.6V_{\text{s}} = 18$ km s⁻¹). The latter is excluded, however, as it predicts a well resolved emission thickness of 64 AU = 0'.45 (FWHM) in H₂ 1–0 S(1), while images and toy models indicate a barely resolved rim $\leq 0'.1$. Note that this does not exclude a strongly magnetized wind with $b > 0.1$. All C-shock models in Table 1 assume a preshock ionization from cosmic rays alone, as appropriate for ambient gas. But a molecular wind launched

within 10 AU is irradiated by stellar FUV photons and X-rays and will reach a higher ionization $\approx 10^{-4}$ that remains “frozen-in” as the wind expands (e.g., Glassgold et al. 1991; Panoglou et al. 2012). A J-shock will then result even if $b > 0.1$, due to the strong ion-neutral coupling. The required J-shock speed and/or preshock density would just increase with b , to compensate for the reduced post-shock compression (higher magnetic pressure).

A definite advantage of the “reverse shock” scenario, compared to the “forward shock” discussed previously, is that the required shock speed can be reached even with a static cavity ($V_{\text{exp}} = 0$) by adjusting $V_{\text{w}\perp}$. This would allow a lower proper motion than the current upper limit of 12 km s⁻¹, and an older cavity age than the 15 yr implied in the forward shock case. A second advantage is that the (conserved) wind component parallel to the shock, $V_{\text{w}\parallel}$, naturally tends to produce blueshifted H₂ centroid velocities; these will be compatible with observations if $V_{\text{w}\parallel} - V_{\perp} \approx 5$ km s⁻¹ (see Sect. 4.2).

Despite its advantages, a serious caveat with the reverse-shock scenario is that the required wind mass flux seems excessive. Since the shock emitting in H₂ 1–0 S(1) is the wind-shock, the one-sided mass flux \dot{M}_{w} intercepted by the shock surface is directly given by

$$\dot{M}_{\text{w}} = (\mu m_{\text{H}} A_{\text{s}}) n_{\text{H}} V_{\text{w}\perp} \quad (7)$$

$$= 6.7 \times 10^{-8} \frac{n_{\text{H}}}{10^6 \text{ cm}^{-3}} \frac{V_{\text{w}\perp}}{10 \text{ km s}^{-1}} M_{\odot} \text{ yr}^{-1}, \quad (8)$$

where we took again a shock area $A_{\text{s}} \approx 2 \times 10^{30} \text{ cm}^2$. The scalings are for the minimum possible values of n_{H} and $V_{\text{w}\perp}$, corresponding to the case $b = 0.1$ and $V_{\text{exp}} = 0$. This lower limit is already uncomfortably close to the DG Tau accretion rate, given that the result should be doubled to account for the occulted red lobe of the wind. A higher b in the wind would require a higher preshock density and/or shock speed and thus an even larger \dot{M}_{w} . The value of $V_{\text{w}\perp}$ would also double if the cavity expands at $V_{\text{exp}} = 10$ km s⁻¹ instead of being static.

We conclude that the “reverse shock” scenario for the origin of the wide-angle H₂ $v = 1\text{--}0$ emission in DG Tau has several attractive features compared to a forward shock (possibility of a static cavity, naturally blueshifted centroids). However, it appears to require an excessive wind mass flux compared to current accretion rates in DG Tau.

5. Conclusions

We have conducted a thorough analysis of H₂ 1–0 S(1) spectro-imaging data towards the classical T Tauri star DG Tau, with an angular resolution of 0'.12 and a precision in velocity centroids reaching down to a few km s⁻¹. We compared the morphology and kinematics with simultaneous data in [Fe II] (Agra-Amboage et al. 2011), near-contemporaneous spectra in [O I] (Coffey et al. 2007), and spectra and images in FUV-pumped H₂ obtained 6 years later (Schneider et al. 2013b,a). The absolute line brightness and the 2–1 S(1)/1–0 S(1) ratio were used to constrain shock conditions, based on state-of-the-art shock models (Kristensen et al. 2008). Projection effects in radial velocities were modeled to constrain the intrinsic velocity field of the emitting gas. This new information was used to re-examine proposed origins for the wide-angle H₂ emission in the blue lobe of DG Tau and similar sources. Our main conclusions, and our suggestions for further work, are the following:

- The faint arc of H₂ 1–0 S(1) emission in the red lobe traces slow material at $+5$ km s⁻¹ in the wings of a large bow-shock prominent in [Fe II]. In contrast, the limb-brightened

H₂ 1–0 S(1) at the base of the blue lobe is much wider than the [Fe II] jet; it appears filled-in by the wide-angle atomic wind at low velocities seen in [O I] and [S II], that is, steady over ≥ 4 yr but invisible in [Fe II] probably because of strong iron depletion. Most of the wide-angle H₂ 1–0 S(1) is at low blueshifts (between -5 and 0 km s⁻¹). Hence, we confirm previous claims that the H₂ blue lobe in DG Tau appears as a slower, wider extension of the nested velocity structure previously observed in atomic lines (Takami et al. 2004; Schneider et al. 2013a). The H₂ may be rotating about the jet axis in the same sense as the disc and atomic flow, with $V_\phi \leq 7$ km s⁻¹.

- The blue lobe morphology in H₂ 1–0 S(1) is strikingly similar to the FUV image (Schneider et al. 2013a), confirming that they trace the same hot gas at 2000 K and setting upper limits on the rim thickness ≤ 14 AU and on any expansion proper motion $V_{\text{exp}} < 12$ km s⁻¹. The face-on surface brightness in 1–0 S(1) is $\approx 3 \times 10^{-3}$ erg s⁻¹ cm⁻² sr⁻¹, and the 2–1 S(1)/1–0 S(1) ratio is uniform at our resolution. If due to shock-heating, they require a J-shock at 10 km s⁻¹ into 10⁶ cm⁻³ gas (C-shocks would predict excessive rim thickness). Modeling of the radial velocities limits the gas motion perpendicular to the walls to $-5 \leq V_\perp \leq +5$ km s⁻¹, unless there is a comparable parallel component in which case V_\perp can reach 20 km s⁻¹.
- A photoevaporating disc atmosphere irradiated by the strong stellar FUV excess and Ly α from jet shocks seems able to explain the excitation and brightness on observed scales, as well as the low blueshifts over most of the area. One caveat is the high density in the upper disc atmosphere of $n_{\text{H}} = 10^7$ cm⁻³ suggested by steady PDR models. Time-dependent PDR models including disc photoevaporation may alleviate this problem and would be highly desirable.
- A molecular MHD disc wind launched around 10 AU and heated by ambipolar diffusion is another promising scenario that can reproduce the observed morphology, kinematics (including limits on rotation), mass flux rate, and temperature (see Panoglou et al. 2012). Synthetic predictions in H₂ 1–0 S(1) taking into account non-LTE effects, the full 3D velocity field, and a range of streamlines are necessary to fully test this hypothesis and will be the subject of future work.
- A cavity of shocked ambient swept-up gas does not reproduce the H₂ 1–0 S(1) excitation and blueshifted centroids unless it is very young (15 yr) and expands into a pre-existing dense molecular wind of unclear origin moving at ≈ 15 km s⁻¹ along the cavity walls. A crucial check of this scenario would be to detect the predicted proper motion $V_{\text{exp}} \approx 10$ km s⁻¹, and the signs of deceleration or recurrence expected for such an episodic phenomenon.
- A reverse shock into a wide-angle molecular wind could readily explain the excitation, low blueshifts, and apparent stationarity of the H₂ cavity, but the required one-sided wind mass flux of $\geq 6.7 \times 10^{-8} M_\odot \text{ yr}^{-1}$ appears excessive compared to current accretion rates in DG Tau.

We point out that the (J-type) shock scenarios predicts a FWHM of only 0.1 AU for the H₂ 1–0 S(1) emitting layer. This is to be compared with a predicted thickness of 7 AU for a static PDR ($N_{\text{H}} \approx 10^{21}$ cm⁻² and $n_{\text{H}} \approx 10^7$ cm⁻³) and 4–14 AU for an MHD disc wind. Spatially resolving the rims of the H₂ cavity would thus bring useful insight into its origin. We also caution that we have considered simplistic scenarios where only one heating mechanism is operating at a time. A combination of shock and

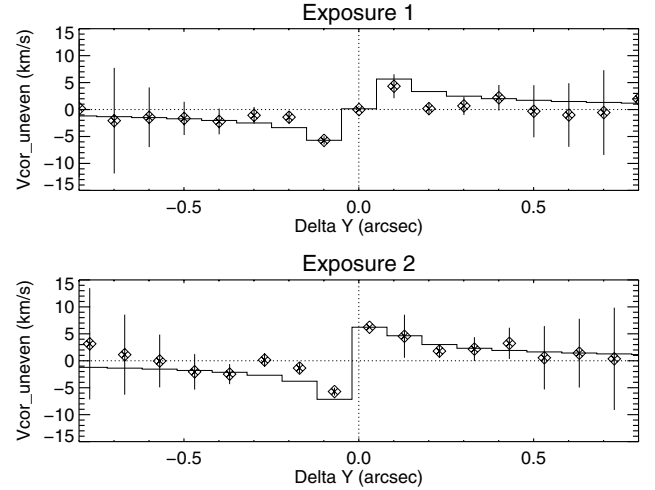


Fig. A.1. Velocity corrections for uneven slit illumination in PV diagrams along the jet averaged ± 0.5 across the jet axis for exposure 1 (top) and exposure 2 (bottom). Black histograms plot the theoretical correction computed for a 2D brightness distribution fitted by a Moffat function. Symbols with error bars show empirical shifts obtained from cross-correlation of telluric absorption features against the reference spectrum (at $Y = 0''$ in exposure 1 and $Y = +0.03''$ in exposure 2). To ease comparison with the theoretical model, they are shifted vertically to match the model at the reference spectrum position.

FUV irradiation might alleviate the caveats encountered when each is considered separately.

Acknowledgements. The authors are grateful to D. Coffey for kindly providing the [O I] transverse slit data shown in Fig. 5, to G. Herczeg for precious advice on velocity calibration, and to the referee, M. Takami, for insightful comments that led to significant improvement of the paper. V. Agra-Amboage acknowledges financial support through the Fundação para a Ciência e Tecnologia (FCT) under contract SFRH/BPD/69670/2010. This research was partially supported by FCT-Portugal through Project PTDC/CTE-AST/116561/2010. The authors also acknowledge financial and travel support through the Marie Curie Research Training Network JETSET (Jet simulations, Experiments and Theory) under contract MRTN-CT-2004-005592, and through the french Programme National de Physique Stellaire (PNPS).

Appendix A: Correction of SINFONI data for uneven slit illumination

We obtain an empirical estimate of the uneven-slit illumination effect in our *K*-band data by noting that telluric absorption features will be subject to the same spurious shifts as the H₂ lines, since the light distribution in the slitlet is dominated by the stellar continuum in both cases. To estimate the shifts in telluric lines as a function of distance from the continuum peak, we increase S/N by constructing a PV diagram along the jet, averaging spaxels over a width ± 0.5 across the jet axis (i.e., along each slicing mirror). We then cross-correlate each of these PV spectra with the spectrum closest to the DG Tau position, over an interval of $0.06 \mu\text{m}$ left of the H₂ line that shows numerous telluric absorption features. The resulting empirical shifts in each exposure are plotted as diamond symbols in Fig. A.1. It may be seen that the effect is $\approx \pm 5$ km s⁻¹ for the slitlets within ± 0.1 of the source and drops to ≤ 2 km s⁻¹ beyond this region. We also modeled the uneven-slit illumination effect for each exposure following the formulation developed by Marconi et al. (2003), using a Moffat function fitted to the corresponding continuum image to represent the 2D light distribution delivered by the AO. The modeled velocity correction is overplotted as black

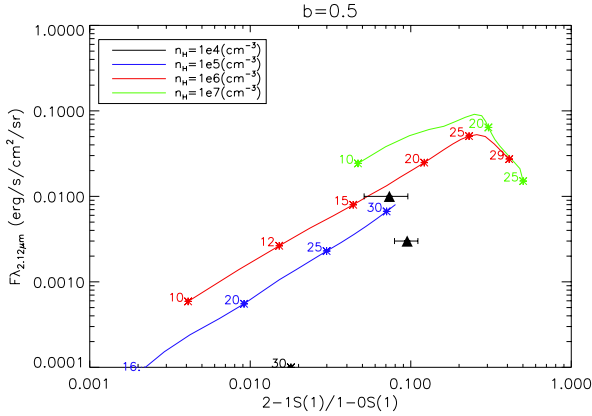


Fig. B.1. The H_2 brightness in the $v = 1-0$ S(1) 2.12 μm line against the $v = 2-1$ S(1)/ $v = 1-0$ S(1) ratio for two positions in the DG Tau blue lobe (filled triangles with error bars) and for the grid of planar C-shock models with $b = 0.5$ (color curves) calculated by Kristensen et al. (2008). Each curve corresponds to a different value of the preshock hydrogen nucleus density, increasing from bottom to top: $n_{\text{H}} = 10^4$, 10^5 , 10^6 and 10^7 cm^{-3} . The shock speed V_s increases to the right and some values are marked along the curves to guide the eye.

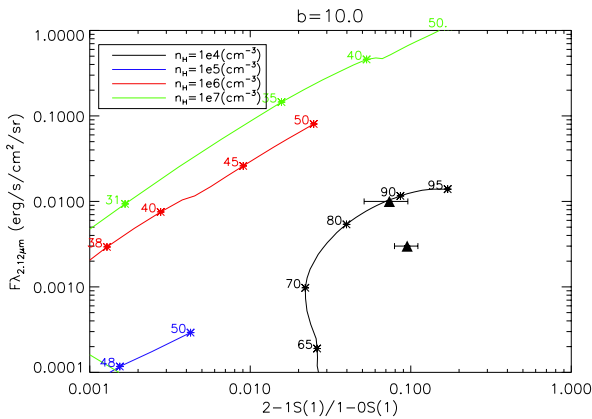


Fig. B.2. Same as Fig. B.1 but for a grid of C-shocks with $b = 10.0$.

histograms in Fig. A.1. The agreement with the velocity shifts obtained by cross-correlation is seen to be very good, with a maximum deviation ≈ 2.0 km s^{-1} within $\pm 0'.3$ of the star and compatible with zero further out. We therefore use this 2D illumination model to correct for uneven slit illumination the H_2 velocity centroids in each individual spaxel (Fig. 3), in the PV diagram along the jet (Fig. 4), and in a transverse PV-diagram across the jet (Fig. 5). We expect residual systematic errors in the corrected velocities of at most 2 km s^{-1} within $\pm 0'.3$ of the star and less than this further out, where the effect anyway becomes quite small.

Appendix B: Shock models

The grid of shock models computed by Kristensen et al. (2008) provides the expected H_2 line fluxes for different input values of n_{H} , V_s , and magnetic field parameter b . Comparing the observed $v = 1-0$ S(1) brightness and $v = 2-1$ S(1)/ $v = 1-0$ S(1) ratio with those predicted, the preshock density and shock velocity can be derived, depending on the magnetic field. These constraints are used in Sect. 4 to discuss scenarios involving shocks for the origin of the H_2 emission in DG Tau. We presented

in Fig. 7 the model predictions for J-shocks with $b = 0.1$ and C-shocks with $b = 1$, as an example. Here we present in Figs. B.1 and B.2 similar model predictions for $b = 0.5$ and $b = 10$, two extreme cases that give a more complete view of the behavior of these models and explain the results shown in Table 1.

References

- Agra-Amboage, V., Dougados, C., Cabrit, S., Garcia, P. J. V., & Ferruit, P. 2009, A&A, 493, 1029
- Agra-Amboage, V., Dougados, C., Cabrit, S., & Reunanen, J. 2011, A&A, 532, A59
- Anderson, J. M., Li, Z.-Y., Krasnopolsky, R., & Blandford, R. D. 2003, ApJ, 590, L107
- Arce, H. G., Shepherd, D., Gueth, F., et al. 2007, in Protostars and Planets V (Tucson: University of Arizona Press), 245
- Ardila, D. R., Basri, G., Walter, F. M., Valentí, J. A., & Johns-Krull, C. M. 2002, ApJ, 566, 1100
- Bacciotti, F., Mundt, R., Ray, T. P., et al. 2000, ApJ, 537, L49
- Bacciotti, F., Ray, T. P., Mundt, R., Eisloffel, J., & Solf, J. 2002, ApJ, 576, 222
- Bai, X.-N. 2013, ApJ, 772, 96
- Bai, X.-N., & Stone, J. M. 2013, ApJ, 769, 76
- Bally, J., Reipurth, B., & Davis, C. J. 2007, in Protostars and Planets V, eds. B. Reipurth, D. Jewitt, & K. Keil (Tucson: University of Arizona Press), 215
- Bary, J. S., Weintraub, D. A., & Kastner, J. H. 2003, ApJ, 586, 1136
- Bast, J. E., Brown, J. M., Herczeg, G. J., van Dishoeck, E. F., & Pontoppidan, K. M. 2011, A&A, 527, A119
- Beck, T. L., McGregor, P. J., Takami, M., & Pyo, T.-S. 2008, ApJ, 676, 472
- Bonnet, H., Conzelmann, R., Delabre, B., et al. 2004, in Proc. SPIE 5490, eds. D. Bonaccini Calia, B. L. Ellerbroek, & R. Ragazzoni, 130
- Bontemps, S., André, P., Terebey, S., & Cabrit, S. 1996, A&A, 311, 858
- Burton, M. G., Hollenbach, D. J., & Tielens, A. G. G. M. 1990, ApJ, 365, 620
- Cabrit, S., Edwards, S., Strom, S. E., & Strom, K. M. 1990, ApJ, 354, 687
- Carmona, A., van der Plas, G., van den Ancker, M. E., et al. 2011, J. A&A, 533, A39
- Casse, F., & Ferreira, J. 2000, A&A, 361, 1178
- Coffey, D., Bacciotti, F., Ray, T. P., Eisloffel, J., & Woitas, J. 2007, ApJ, 663, 350
- Coffey, D., Bacciotti, F., & Podio, L. 2008, ApJ, 689, 1112
- Davis, C. J., Stern, L., Ray, T. P., & Chrysostomou, A. 2002, A&A, 382, 1021
- Davis, C. J., Cervantes, B., Nisini, B., et al. 2011, A&A, 528, A3
- Delamarter, G., Frank, A., & Hartmann, L. 2000, ApJ, 530, 923
- Dullemond, C. P., Hollenbach, D., Kamp, I., & D'Alessio, P. 2007, in Protostars and Planets V, eds. B. Reipurth, D. Jewitt, & K. Keil (Tucson: University of Arizona Press), 555
- Eisenhauer, F., Abuter, R., Bickert, K., et al. 2003, in Proc. SPIE 4841, eds. M. Iye, & A. F. M. Moorwood, 1548
- Ferreira, J., Dougados, C., & Cabrit, S. 2006, A&A, 453, 785
- Fischer, W., Edwards, S., Hillenbrand, L., & Kwan, J. 2011, ApJ, 730, 73
- Font, A. S., McCarthy, I. G., Johnstone, D., & Ballantyne, D. R. 2004, ApJ, 607, 890
- France, K., Schindhelm, E., Herczeg, G. J., et al. 2012, ApJ, 756, 171
- Fromang, S., Terquem, C., & Nelson, R. P. 2005, MNRAS, 363, 943
- García-Díaz, M. T., López, J. A., García-Segura, G., Richer, M. G., & Steffen, W. 2008, ApJ, 676, 402
- García-Segura, G., López, J. A., & Franco, J. 2005, ApJ, 618, 919
- Glassgold, A. E., Mamon, G. A., & Huggins, P. J. 1991, ApJ, 373, 254
- Greene, T. P., Barsony, M., & Weintraub, D. A. 2010, ApJ, 725, 1100
- Gullbring, E., Calvet, N., Muzerolle, J., & Hartmann, L. 2000, ApJ, 544, 927
- Gustafsson, M., Ravkilde, T., Kristensen, L. E., et al. 2010, A&A, 513, A5
- Hartigan, P., Edwards, S., & Ghandour, L. 1995, ApJ, 452, 736
- Herczeg, G. J., Linsky, J. L., Walter, F. M., Gahm, G. F., & Johns-Krull, C. M. 2006, ApJS, 165, 256
- Hollenbach, D., & Natta, A. 1995, ApJ, 455, 133
- Ibgui, L., & Hartmann, J. 2002, J. Quant. Spectr. Rad. Transf., 75, 273
- Ibgui, L., Valentí, A., Merienne, M., et al. 2002, J. Quant. Spectr. Rad. Transf., 74, 401
- Kitamura, Y., Kawabe, R., & Saito, M. 1996, ApJ, 457, 277
- Krist, J. E., Stapelfeldt, K. R., Hester, J. J., et al. 2008, AJ, 136, 1980
- Kristensen, L. E., Ravkilde, T. L., Field, D., Lemaire, J. L., & Pineau des Forêts, G. 2007, A&A, 469, 561
- Kristensen, L. E., Ravkilde, T. L., Pineau des Forêts, G., et al. 2008, A&A, 477, 203
- Lavalley, C., Cabrit, S., Dougados, C., Ferruit, P., & Bacon, R. 1997, A&A, 327, 671

- Lavalley-Fouquet, C., Cabrit, S., & Dougados, C. 2000, *A&A*, 356, L41
- Le Petit, F., Nehmé, C., Le Bourlot, J., & Roueff, E. 2006, *ApJS*, 164, 506
- Marconi, A., Axon, D. J., Capetti, A., et al. 2003, *ApJ*, 586, 868
- Nomura, H., & Millar, T. J. 2005, *A&A*, 438, 923
- Nomura, H., Aikawa, Y., Tsujimoto, M., Nakagawa, Y., & Millar, T. J. 2007, *ApJ*, 661, 334
- Panoglou, D., Cabrit, S., Pineau des Forêts, G., et al. 2012, *A&A*, 538, A2
- Pesenti, N., Dougados, C., Cabrit, S., et al. 2004, *A&A*, 416, L9
- Podio, L., Kamp, I., Codella, C., et al. 2013, *ApJ*, 766, L5
- Porter, J. M., Oudmaijer, R. D., & Baines, D. 2004, *A&A*, 428, 327
- Pudritz, R. E., Ouyed, R., Fendt, C., & Brandenburg, A. 2007, in *Protostars and Planets V*, eds. B. Reipurth, D. Jewitt, & K. Keil (Tucson: University of Arizona Press), 277
- Pyo, T.-S., Kobayashi, N., Hayashi, M., et al. 2003, *ApJ*, 590, 340
- Ray, T., Dougados, C., Bacciotti, F., Eisloffel, J., & Chrysostomou, A. 2007, in *Protostars and Planets V*, eds. B. Reipurth, D. Jewitt, & K. Keil (Tucson: University of Arizona Press), 231
- Rothman, L. S., Gordon, I. E., Barbe, A., et al. 2009, *J. Quant. Spectr. Rad. Transf.*, 110, 533
- Safier, P. N. 1993, *ApJ*, 408, 115
- Schneider, P. C., Eisloffel, J., Güdel, M., et al. 2013a, *A&A*, 557, A110
- Schneider, P. C., Eisloffel, J., Güdel, M., et al. 2013b, *A&A*, 550, L1
- Shang, H., Li, Z.-Y., & Hirano, N. 2007, in *Protostars and Planets V*, eds. B. Reipurth, D. Jewitt, & K. Keil (Tucson: University of Arizona Press), 261
- Smith, M. D. 1995, *A&A*, 296, 789
- Takami, M., Chrysostomou, A., Ray, T. P., et al. 2004, *A&A*, 416, 213
- Takami, M., Beck, T. L., Pyo, T.-S., McGregor, P., & Davis, C. 2007, *ApJ*, 670, L33
- Testi, L., Bacciotti, F., Sargent, A. I., Ray, T. P., & Eisloffel, J. 2002, *A&A*, 394, L31
- Tielens, A. G. G. M., & Hollenbach, D. 1985, *ApJ*, 291, 722
- Valenti, J. A., Johns-Krull, C. M., & Linsky, J. L. 2000, *ApJS*, 129, 399
- Wallace, L., & Hinkle, K. 1996, *ApJS*, 107, 312
- Whelan, E. T., Ray, T. P., Bacciotti, F., et al. 2005, *Nature*, 435, 652